

Reflection processing of crosswell seismic data: Midale field, Saskatchewan

Ashraf A. Abdalla, Robert R. Stewart, and David C. Henley

ABSTRACT

A development study is presented here for the analysis and processing of crosswell seismic data. This work uses direct arrivals and reflections to construct an image. Use of reflections in addition to transmissions promises to provide higher resolution sections.

To this end, high frequency crosswell data, from the Midale field of southeastern Saskatchewan, have been processed for reflections. The data were acquired by Shell Development Company for Shell Canada Ltd. as part of their EOR monitoring studies. Raw field data showed a complex assortment of wave modes that included direct compressional and shear waves, head waves, guided waves, converted transmitted waves and reflected shear waves. A travelttime inversion technique (layer-stripping via raytracing) was developed to obtain P- and S-wave interval velocities from the respective direct arrivals. Further analysis of the receiver-gathered data showed evidence of primary reflected downgoing arrivals as well as the primary reflected upgoing arrivals. Downgoing primary reflections were selected and processed with the upgoing reflections to obtain a subsurface image. The reconstruction method used is similar to conventional VSPCDP mapping. Crosswell geometry is shown to provide an extended subsurface coverage away from the borehole which can complement the interpretation of well logs.

INTRODUCTION

Crosswell experiments use at least two boreholes where receivers are placed at depth in one borehole and source(s) in another. Similar events, upgoing and downgoing, are present in crosswell data as in VSP except that in the crosswell experiment the receiver can be above the source. When the geophone is at the same or near the depth level of the source, waves traveling horizontally also exist in crosswell data. The unique advantage of crosswell data is that the entire source/receiver location is placed beneath the weathered layer and can thus be closer to the zone of interest. This setting avoids some of the loss of high frequencies. The other contributing factor about obtaining the high frequencies is the generally small distance between the boreholes. The energy range in crosswell seismic can be in the kilohertz range which can theoretically resolve layers as thin as .6 m vertically (Iverson, 1988). This is very important for hydrocarbon-reservoir description and development where high resolution is required. The experiment is often used to monitor any Enhanced Oil Recovery (EOR) activity in the area between the boreholes.

Numerical modeling of crosswell data shows that reflected, transmitted, guided, and converted waves are all prominent in crosswell data (Hu et al., 1988b). However, most crosswell studies have only used the direct arrivals to obtain velocity information about the medium between the boreholes using tomographic inversion techniques. Of these studies, Bois et al. (1972) acquired and inverted, via raytracing, the first arrivals of crosswell data in order to detect major structural events. Imaging methods like the algebraic

reconstruction techniques (ART) and the simultaneous iterative reconstruction techniques (SIRT) were respectively used by Peterson et al. (1985) and Ivansson (1985) to estimate seismic velocities for two-dimensional (2-D) models in the presence of low-velocity zones. Least-squares inversion techniques, that produced 2-D models of compressional seismic velocities between two boreholes, have also implemented to detect low-velocity regions associated with heavy fracturing, and steam injection and fire-flood zones (Macrides, 1987; Bregman et al., 1989; Justice et al., 1989). The same method helped Lines and LeFehr (1989) to understand better the homogeneity of the subweathering layer, but due to the lack of raypath coverage, the inversion results could not help them to understand the weathered zone. Other applications of first arrivals in crosswell data included diffraction tomography (Pratt and Worthington, 1988) that provided a qualitative image of a wedge anomaly, velocity anisotropy in shale (Winterstein and Paulsson, 1990), and seismic velocity before and after steam injection (Macrides, 1987).

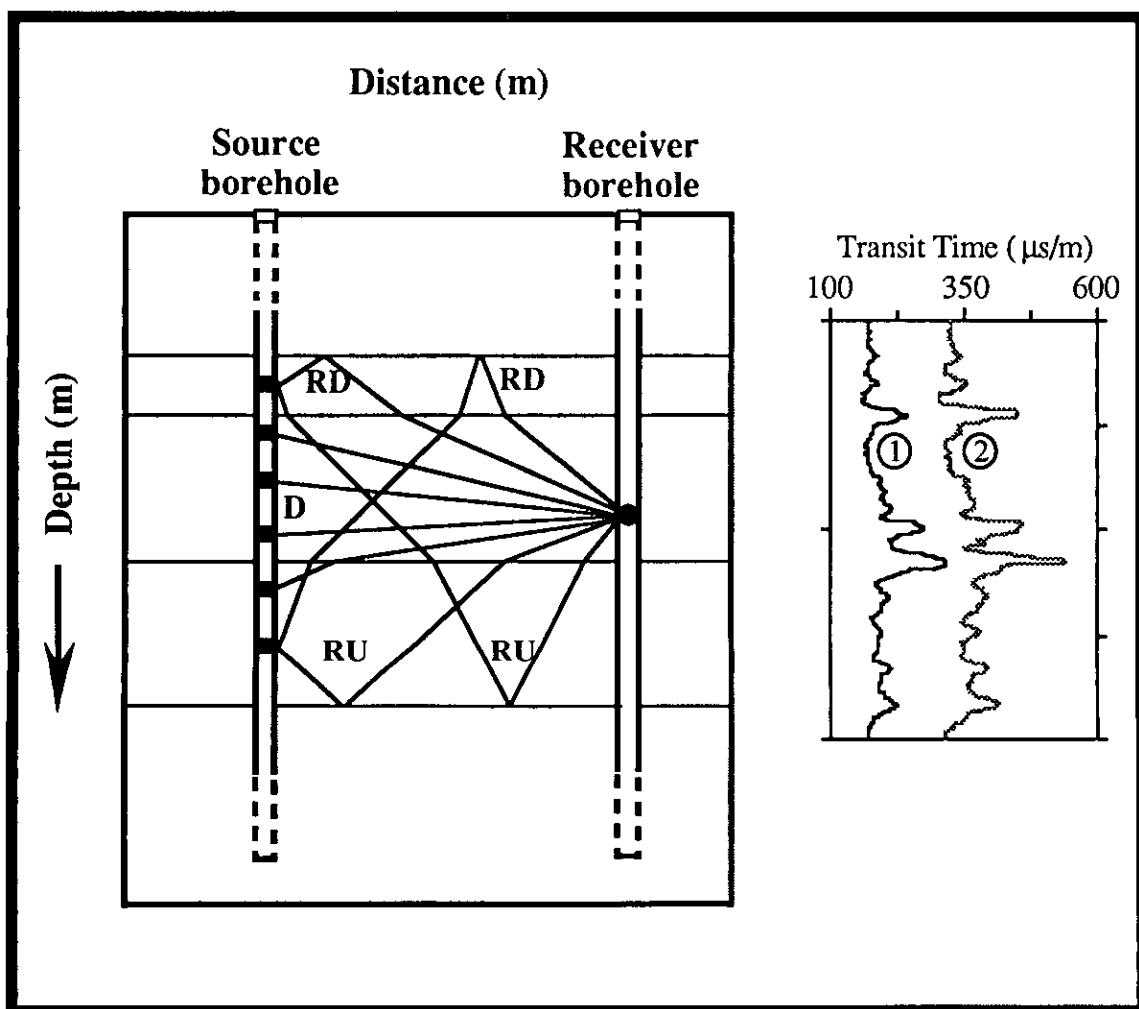


Figure 1: Crosswell geometry suggests the use of direct arrivals in estimating velocities, and reflected arrivals in obtaining a reflected image in depth. The right part of the Figure shows the compressional, 1, and shear, 2, slownesses of the zone of coverage.

A few studies have considered the different types of scattered waves which constitute the later arrivals in a crosswell seismic record. Of these studies, acoustic modeling and imaging of crosswell data with finite-differences were presented by Hu et al. (1988a), for common-source gathers (prestack), and by Zhu and McMechan (1988), for stacked data. In those studies, the reverse-time wave equation method was used to obtain a depth section from the total wavefield. Another 2-D migration/inversion technique by Beydoun et al. (1989) produced elastic (velocity and density) maps of the subsurface from the full waveform.

Only a few authors (e.g. Baker and Harris, 1984; Iverson, 1988) have considered reflection processing of crosswell data by a method more similar to conventional CDP and VSP processing. The final product of these two studies was a depth section similar to the classic CDP seismogram recorded on the surface for exploration purposes. An expanded study (Abdalla and Stewart, 1989) considered this method for synthetic crosswell seismic data and offered insights into the subsurface coverage and the multi-layered transformation technique of crosswell data.

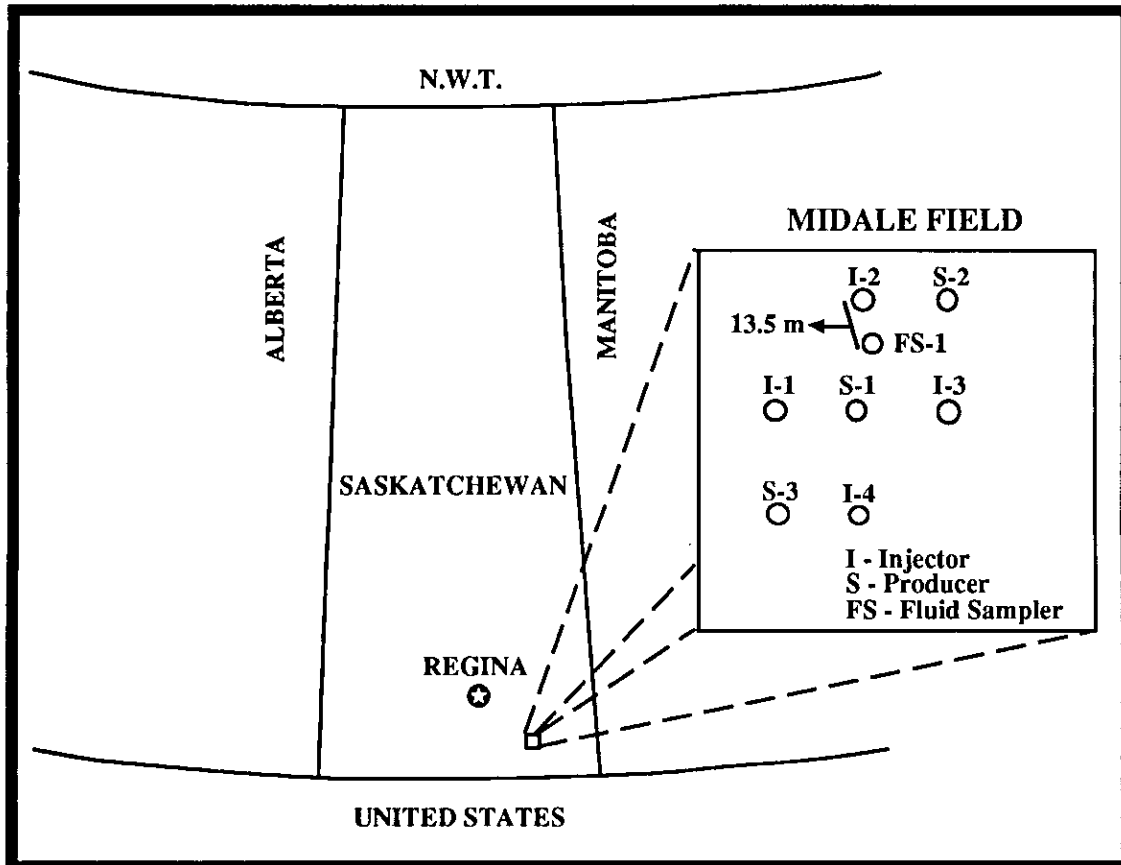


Figure 2: Study area of the field crosswell data. The experiment was conducted between FS-1, source well, and I-2, receiver well. The distance between the boreholes is 13.5 m.

OBJECTIVES

The overall objective of this study is to exploit the full waveform of crosswell data and deduce information about the geology in terms of velocity and reflectivity of the subsurface between the boreholes. This starts with further understanding of wave propagation and type of geometry crosswell data exhibit. Secondly, a one-dimensional (1-D) solution of the velocity function is sought from the direct arrivals, **D**, of crosswell data (Figure 1). The following objective is perhaps challenging in that it is unfamiliar to most of the research efforts paid to crosswell data. That is, focusing on developing a processing flow of the later arrivals, reflected events **RD** and **RU**, rather than the direct ones to obtain a reflected image in depth of the covered zone between the boreholes (Figure 1). Finally, as the ultimate goal of every processing study, the ability to interpret such reflected image is to be discussed and presented.

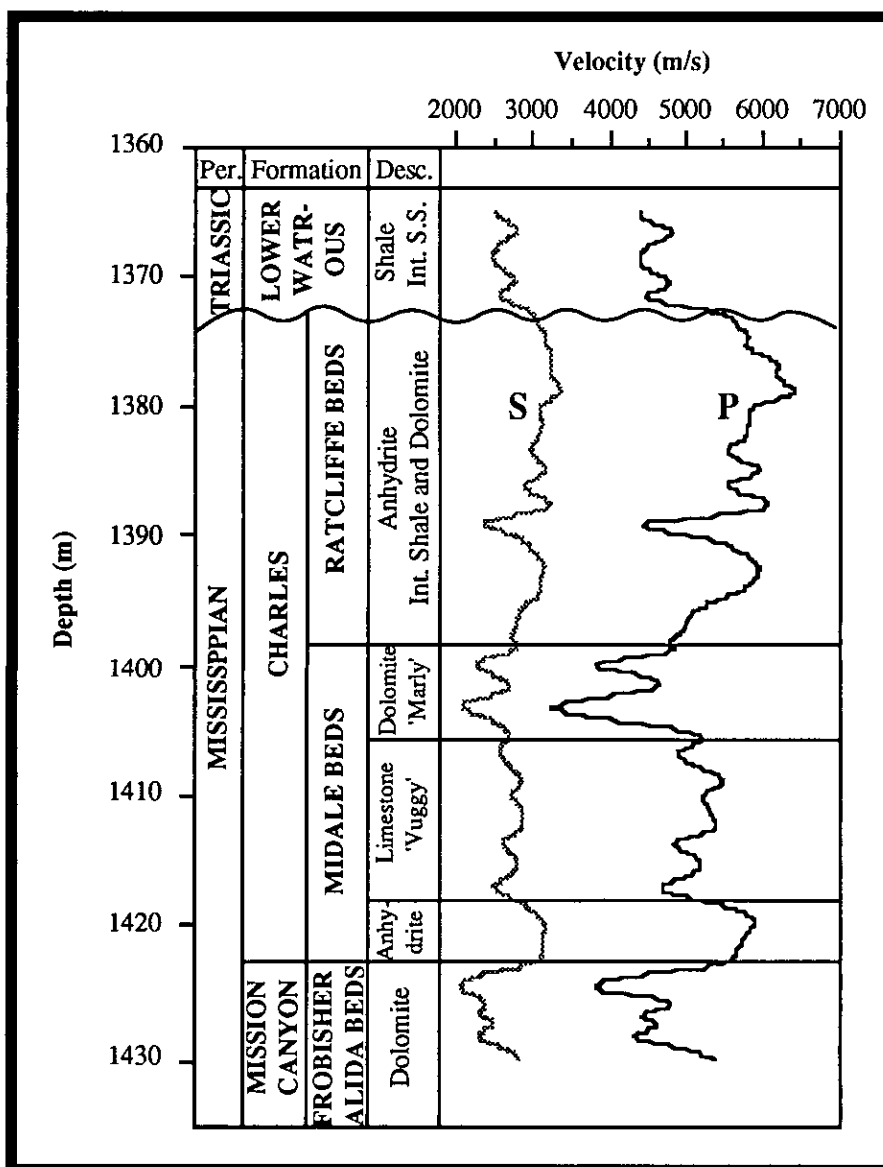


Figure 3: Regional stratigraphy of the Midale field.

GEOLOGY AND SURVEY

Study area

The study area is located in the Midale field of southeastern Saskatchewan about 150 km southeast of Regina (Figure 2). The crosswell experiment considered in this study was conducted between a fluid sampling well (FS-1) and an injector well (I-2) during an EOR monitoring activity. The source was placed in the FS-1 well while the receiver was in the I-2 well. The distance between the boreholes is 13.5 m (Figure 2) while the zone of interest extends from 1380 m to 1420 m. The stratigraphic column of the area (Figure 3) is shown for the interval from 1365 m to 1430 m. There are two productive zones, a marly porous dolomite (upper) and a vuggy porous limestone (lower), of the Midale formation. The Ratcliffe beds (shale and dolomite interbedded anhydrite) overlie the Midale strata. Below the productive layers, there is an anhydrite zone which overlies the Frobisher Alida formation, another porous dolomite zone in the area but is water bearing.

Field data

Shell Development Company acquired the data for Shell Canada Ltd. in 1985 as part of their EOR monitoring studies. The data are of the receiver-gather type with the following parameters:

Distance between boreholes:	13.5 m
Number of sources/receiver:	variable (average of 400)
Source depths:	1371.1 m (min.) - 1440.2 m (max.)
Source spacing:	0.1 m
Number of receivers:	9 (numbered 1 to 9)
Receiver depths:	1390.8, 1392.0, 1393.5, 1398.0, 1399.0, 1401.0, 1418.5, 1419.0, 1420.0
Sampling interval:	8 μ s

The source used in the experiment was of a magnetostrictive type that had a centre frequency of about 20 kHz. The receiver was a hydrophone. Both source and receiver were suspended in fluid-filled, cased boreholes. Unfortunately, there was one serious flaw in the data which is that source/receiver depths could not be confirmed due to problems in the field.

As stated above, there are 9 receiver gathers representing the field component of the data base provided in this study. An example of the recorded gathers (receiver no. 2) is shown in Figure 4. Receiver depth is 1392 m while sources are shown from depth 1376 m to 1405 m (291 traces). The maximum recorded time is 9.6 ms with sampling interval of 8 μ s (1200 samples). The experiment was conducted for transmission purposes; that is, focusing on the direct arrivals only. The data stored on tape were limited to a maximum of 1200 samples. This represents a considerable disadvantage in these data since the major objective is to use the reflections that arrive at a later time in the recorded data.

The data example shown in Figure 4 is the result of a band-pass filter and a trace-equalization process. The high-frequency signals are found to have bandwidths of 2.5 kHz

to 17.25 kHz. Although the magnetostrictive source and the hydrophone used in this experiment respectively generate and record only P waves, P to S and S to P conversions at the borehole walls enable the study of S waves as well as P waves. The same conversion observation was noticed by Fehler and Pearson (1984). For example, direct P- and S-wave arrivals are labeled D-P and D-S as well as reflected upgoing and downgoing shear wave arrivals, RUSS and RDSS respectively. Note the strong amplitudes of the direct shear waves in Figure 4. Fehler and Pearson (1984) derived the expressions of radiation pattern for P and S waves emitted by seismic sources or acoustic transducers in fluid-filled boreholes. The results of their derivations showed much larger S-wave amplitudes than those of P waves. Beydoun et al. (1989) observed similar radiation patterns of larger S waves in crosswell data set recorded on both geophones and hydrophones. Other examples of strong shear waves include hydrophone recorded VSP (Marzetta et al., 1988) and full-waveform sonic data (Hornby, 1989).

A median filter (discussed later in reflection processing) was designed on the direct P-wave mode to enhance this arrival. This enhanced event was subtracted from the original data to reveal the residual events. No significant P-wave reflections were found. The reflected data are dominated by S waves in the form S-S and possibly S-P raypaths. It is apparent that the acquisition geometry with its large angles of incidence favors shear-wave conversions (Beydoun et al., 1989). The use of P waves in this paper will be limited to the inversion of direct P traveltimes arrivals.

DATA PROCESSING

1. Traveltime inversion

The majority of crosswell studies have concentrated on tomographic inversion methods that use the direct arrivals to construct 2-D models in terms of seismic velocities, mostly compressional waves, between two boreholes (Bois et al., 1972; Peterson et al., 1985; Ivansson, 1985; Macrides et al., 1988; Bregman et al., 1989a; Justice et al., 1989; Lines and LeFehr, 1989).

The objective here is to use both P- and S-wave direct arrivals in these crosswell data and seek P and S velocity information which are usually confined to multicomponent VSP inversions (Esmersoy, 1990). A reasonable estimate of these velocities can be extracted by blocking and interpreting the full waveform sonic log (Figure 5). However, an inversion technique is developed to accurately obtain such interval velocity information for P- and S-wave modes. The method, similar to that of Justice (1986b), is based on layer-stripping via raytracing. The geometrical and theoretical aspects of the method are briefly discussed here followed by field data inversion results.

1.1 Inversion geometry and formulation

Subsurface information about the Midale field in southeastern Saskatchewan and a limited separation between boreholes (13.5 m) in an experiment like the crosswell one led to comfortably assume flat layering for the geologic model on which the inversion procedure is based. Also, as mentioned earlier, a 1-D solution of the velocity function is sought. The given parameters to the inversion program are the geologic model that contains the layering between the boreholes, the experiment geometry (source and receiver locations), and the direct arrival picks of both P- and S-waves. If we let x be the distance

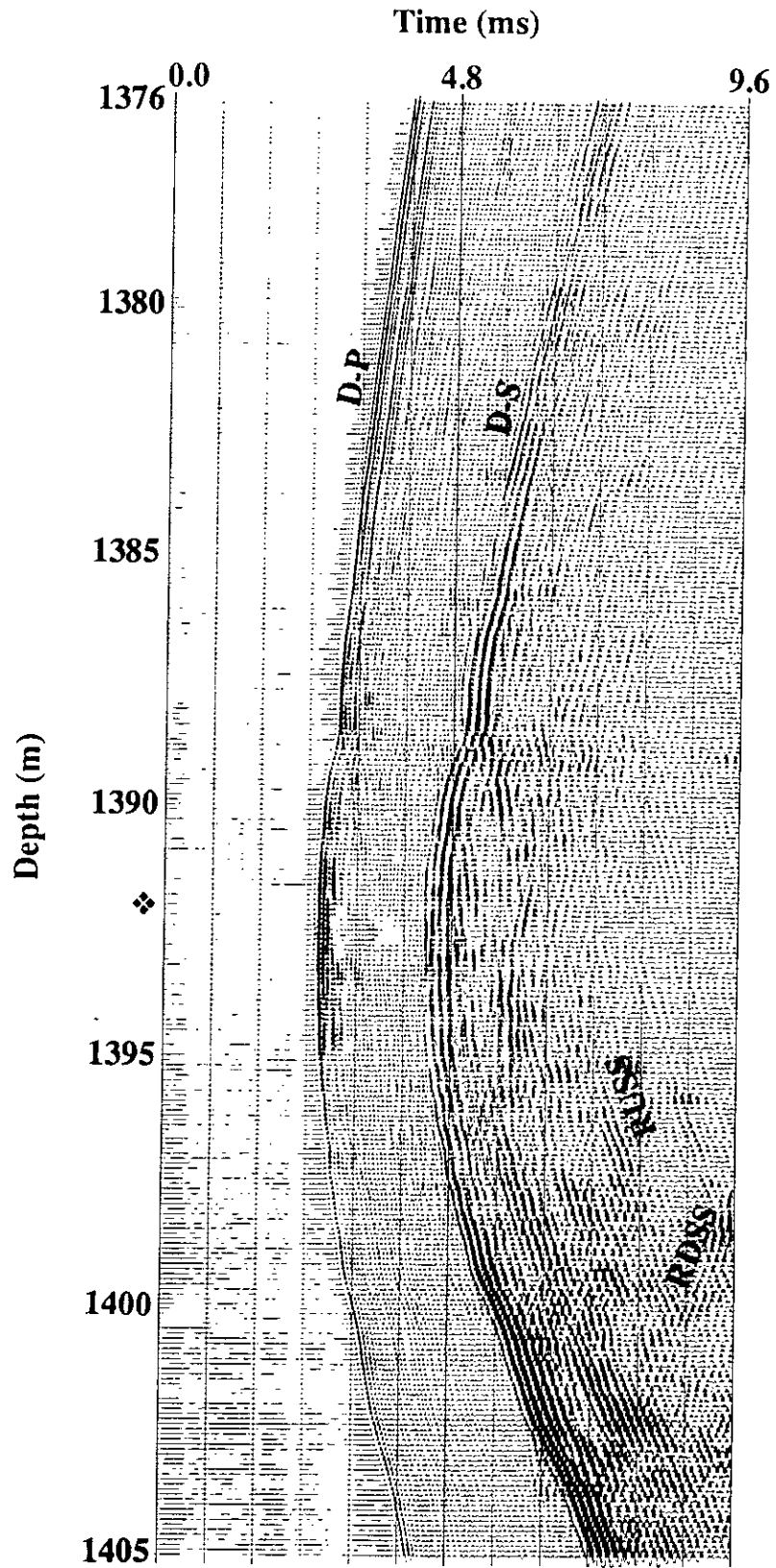


Figure 4: Band-pass receiver gather (no. 2) of the Midale field data. Receiver is at depth 1392 m (star).

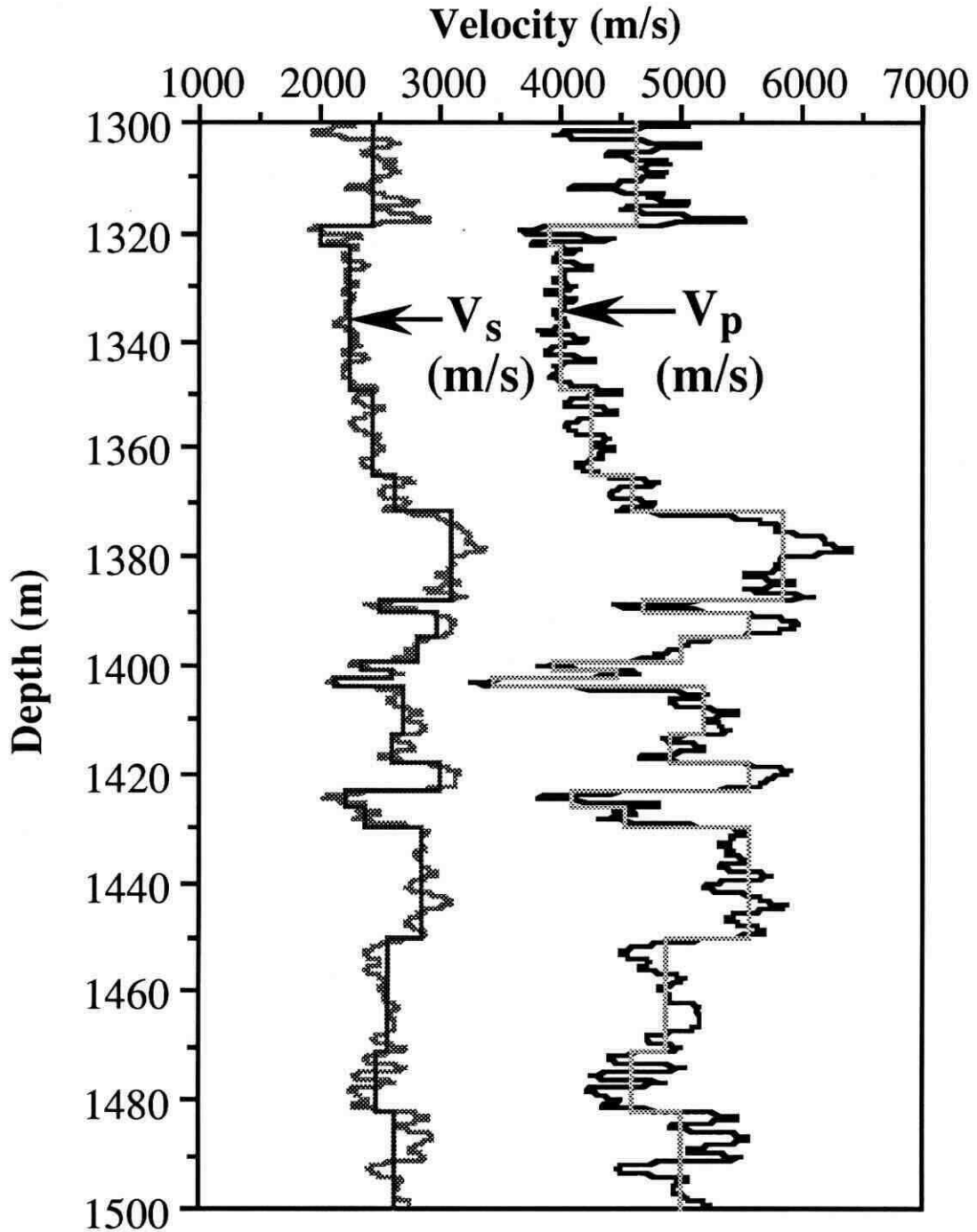


Figure 5: Blocked full-waveform velocity log of the Midale field data.

between the boreholes and t_j^n be the observed travelttime at the receiver in layer n from a shot j in layer i (Figure 6), then it is shown (Slotnik, 1959) that

$$x = \sum_{k=1}^n \frac{p_j v_k \Delta z_k}{[1 - p_j^2 v_k^2]^{\frac{1}{2}}}, \quad (1)$$

and

$$t_j^n = \sum_{k=1}^n \frac{\Delta z_k}{v_k [1 - p_j^2 v_k^2]^{\frac{1}{2}}}, \quad (2)$$

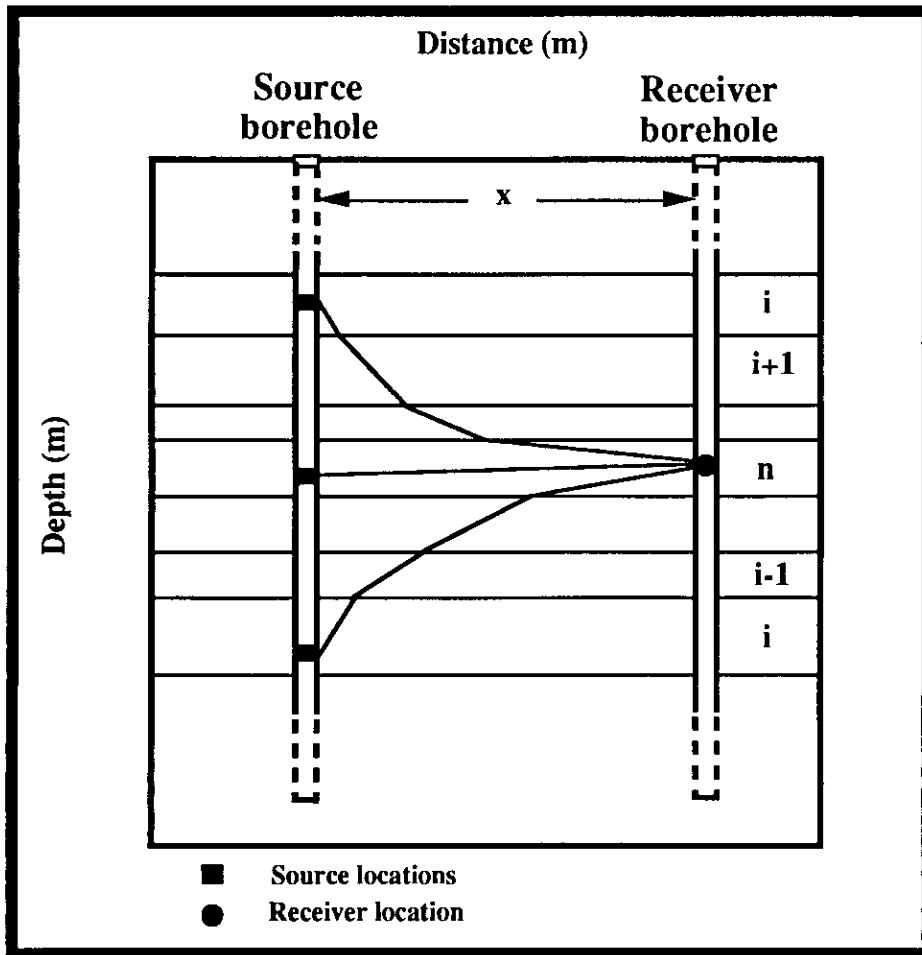


Figure 6: Layer-stripping via raytracing inversion geometry. x is the distance between boreholes. Receiver is in layer n while source is in layer i .

where v_k is the interval velocity of layer k , Δz_k is the vertical distance of the ray in layer k , and p_j is the ray parameter,

$$p_j = \frac{\sin \theta_k}{v_k} = \text{constant}, \quad i \leq k \leq n \quad (3)$$

where θ_k is the angle between the ray in layer k and the vertical.

The algorithm starts solving for the velocity of the interval in which both source and receiver are located. Then, from the receiver layer outward (upward and downward), the program proceeds solving for subsequent intervals using the previously calculated interval velocities. Thus, the method requires at least one direct arrival information in the interval for which the velocity is to be estimated. Also, there would be solutions for the same interval as many sources located in it. This section presents the derivation of the inversion technique and the use of numerical and statistical methods to find the desired solution.

There are basically two formulations in this inversion via raytracing scheme. A straight raypath calculation is firstly performed to estimate the velocity for the layer in which the receiver and source(s) are located. That is

$$v_n = \frac{\sqrt{\Delta z_n^2 + x^2}}{t_j^0} \quad (4)$$

Note here that the receiver layer n is equal to the shot layer i . Following this estimation, a bending raypath calculation (obeying Snell's law) is applied to all other sources (rays) located in layers outside the receiver layer. An example downgoing raypath from the layer i (source) to layer n (receiver) is shown in Figure 6. It is assumed that the velocities of layers n up to $i+1$ have been solved for and it is desired to solve for the interval velocity of layer i . Also, for simplicity, reciprocity is taken into consideration. That is, the receiver location is taken to be the source one and vice-versa, the source location is acting as the receiver one.

Now, consider the difference terms between the total raypath and the raypath only up to the layer before layer i ,

$$\Delta x_j = x - \sum_{k=n}^{i+1} \frac{p_j v_k \Delta z_k}{[1 - p_j^2 v_k^2]^{\frac{1}{2}}}, \quad (5)$$

and

$$\Delta t_j = t_j^0 - \sum_{k=n}^{i+1} \frac{\Delta z_k}{v_k [1 - p_j^2 v_k^2]^{\frac{1}{2}}}, \quad (6)$$

This means that

$$\Delta x_j = \frac{p_j v_i \Delta z_i}{[1 - p_j^2 v_i^2]^{\frac{1}{2}}}, \quad (7)$$

and

$$\Delta t_j = \frac{\Delta z_i}{v_i [1 - p_j^2 v_i^2]^{\frac{1}{2}}}. \quad (8)$$

Solving for v_1 in dividing (7) by (8)

$$v_1 = \sqrt{\frac{1}{p_j} \frac{\Delta x_j}{\Delta t_j}}, \quad (9)$$

and multiplying (7) and (8) gives

$$\Delta x_j \Delta t_j = \frac{p_j \Delta z_1^2}{1 - p_j^2 v_1^2}, \quad (10)$$

$$\Rightarrow \Delta z_1 = \sqrt{\Delta x_j \Delta t_j p_j^{-1} - \Delta x_j \Delta t_j p_j v_1^2}. \quad (11)$$

Replacing (9) in (11)

$$\Delta z_1 = \sqrt{\Delta x_j \Delta t_j p_j^{-1} - \Delta x_j^2}. \quad (12)$$

The term Δz_1 is known since the geologic model and source locations are given parameters to the inversion procedure. The idea here is to estimate p_j that can be used in computing Δx_j and Δt_j in (5) and (6) respectively such that equation (12) holds. Once this is achieved, the raypath is proved to be completed and the interval velocity can be directly obtained from equation (9).

Consider the error function

$$E(p) = \Delta z_1 - \Delta z_1(p), \quad (13)$$

where Δz_1 is the known term and $\Delta z_1(p)$ is the term computed from the estimated p . That is

$$\Delta z_1(p) = \sqrt{\Delta x_j \Delta t_j p^{-1} - \Delta x_j^2}. \quad (14)$$

We require a solution for the equation

$$E(p) = 0, \quad (15)$$

where p is a root of the function E . To find that root, Newton-Raphson (Newton's) method is implemented (Hamming, 1971; Burden and Faires, 1985). The idea behind the method is to fit a tangent line to the curve of the function at the point of the current estimate p_n of the zero. The formula

$$p_{n+1} = p_n - \frac{E(p_n)}{E'(p_n)}, \quad (16)$$

provides a method of going from one guess \mathbf{p}_n to the next guess \mathbf{p}_{n+1} . Analytical evaluation of equation (16) involves differentiating the nonlinear relation between $\Delta z_i(\mathbf{p})$ and \mathbf{p} since Δx_j and Δt_j (equations (5) and (6)) are functions of \mathbf{p} themselves. Undertaking this procedure results the equation

$$\mathbf{p}_{n+1} = \mathbf{p}_n - \frac{2 \left[\Delta z_i \gamma \frac{1}{2} - \gamma \right]}{\left[\Delta x_j \Delta t_j \mathbf{p}^{-2} + \gamma \Delta x_j^{-1} \sum_{k=n}^{i+1} \frac{v_k \Delta z_k}{[1 - \mathbf{p}^2 v_k^2]^{\frac{3}{2}}} \right]} \quad (17)$$

where $\gamma = \Delta x_j \Delta t_j \mathbf{p}^{-1} - \Delta x_j^2$.

In an iteration, the current estimate of the ray parameter is used to evaluate $\Delta z_i(\mathbf{p})$ (equation (14)) by calculating Δx_j and Δt_j . Then, a check for satisfying the capturing of the raypath is performed by equation (13) where we require a tolerance of 0.1 cm (1 mm) to consider the ray captured at the receiver location. If the error tolerance is not met then the next iteration is undertaken and so forth until the ray is captured with the required tolerance. Note that the solution of the interval velocity is directly obtained from equation (9) once the ray parameter is accurately estimated. This may be seen as an appealing feature of this method over the least-squares methods which involve matrix inversions and model velocities perturbations to fit the arrival times.

If there is more than one solution for the interval velocity (more than one source per layer), then the median of the velocity values after sorting them is selected to be the representative velocity of that interval. That is if the number of values was odd. If the number was even, then the mean of the two middle values is taken to be the interval velocity. The decision of selecting the median value was taken among other choices of computing the mean of all values and the mean of a selection of values based on 1.28 standard deviation interval.

1.2 Inversion results

The critical dependence of traveltime inversion on the timing picks has led to only consider the first three gathers of the crosswell data. This is due to the coherent and continuous arrivals present in the first group of gathers rather than those present in the rest of the data. One input component to the inversion algorithm is a depth model of the subsurface layering that contains source/receiver locations. From the source locations of the three considered gathers, the depth model extends from 1372 m to 1413 m. The model boundaries (layer interfaces) were then obtained using the full-waveform sonic information along with the prior information, provided by Shell Canada staff, about the lithology of the subsurface in the area. The top of the model is composed of the Ratcliffe beds, generally anhydrite interbedded with a thin shale layer, then the upper Midale beds, dolomite, followed by the lower Midale beds, limestone.

Inverting the P- and S-wave arrivals of the three receiver gathers independently and overlaying the results according to the model boundaries gives Figures 7 and 8 respectively. The algorithm generally takes 3 iterations to converge. Very few minutes (less than 2) are needed to compute the velocities for an average of 390 points on a Zenith-AT personal computer. One observation here is the consistency of the independent results in

both wave types inversion. In every interval of both cases, the estimated velocities lie within a reasonable range (around 200 m/s) except the thin shale interval (1388 m - 1390 m) in the S-wave inversion (Figure 8) where one estimate was significantly faster than the other two estimates. Ultimately, the median value of every three estimates in the same zone would be selected to represent the velocity of this interval.

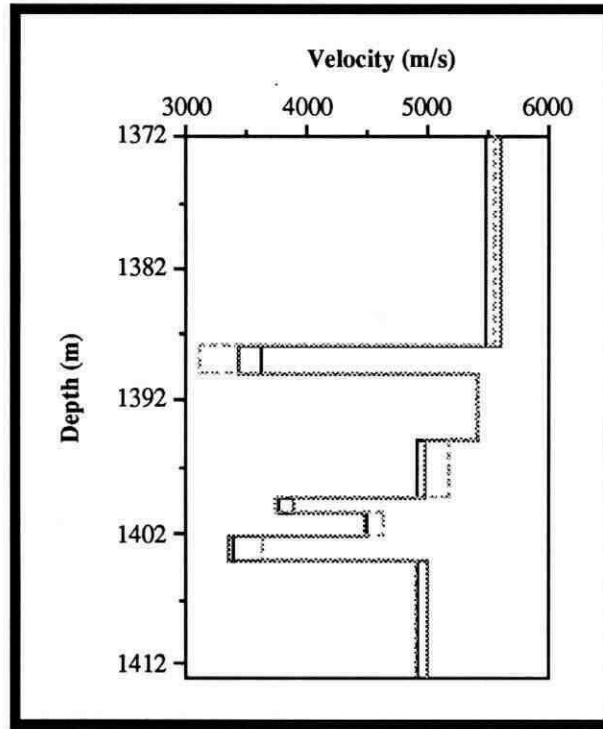


Figure 7: P-wave inversion of three independent receiver gathers

To evaluate the inversion solutions, the constructed 1-D P- and S-wave interval velocity functions are displayed against the full-waveform velocity log recorded in well FS-1 (Figure 9) where the sources were placed. There is a quite good agreement between the seismic and the sonic velocities in all the zones of the model except that thin shale layer again. Had we chosen the faster velocity estimates in both P- and S-wave inversions of that interval, a closer, still slower, agreement with the log would have been obtained. But that would not be consistent with the median selection scheme. The algorithm used here does not appear to have an instability problem in thin layer cases. Every interval of the upper Midale formation (1399 m - 1404 m) has less thickness than that of the shale layer. However, the estimated velocities of these intervals are well in the range of the sonic velocities. The direct explanation to that difference of velocity is not completely known. However, a series of possible factors can be contributing to its presence. Firstly, core samples taken from well FS-1 by Shell Canada suggested that this shale layer has a thickness less than 1 m which led to doubting the sonic readings of this zone as the log might not have resolved it. Secondly, as mentioned in the survey section, the locations of the source/receiver array are not confirmed from the field experiment. This might introduce velocity estimation errors particularly since the locations of the receivers in this group are around 1392 m, very close to the shale layer. Another possible explanation to that velocity discrepancy is that the sonic log depends on the vertical transmissions while the seismic

(crosswell in this case) depends on nearly horizontal transmissions. Since the thin interval is known to be of shale lithology, it gives rise to the known anisotropic property of shale where the velocity in the vertical direction is different from the horizontal direction (Banik, 1984). Finally, it may be that the raypath in this zone is more complex than just direct path from the source to the receiver in which case the used algorithm can give false estimates. However, this is unlikely the problem as it would be shown later in forward modelling and error analysis.

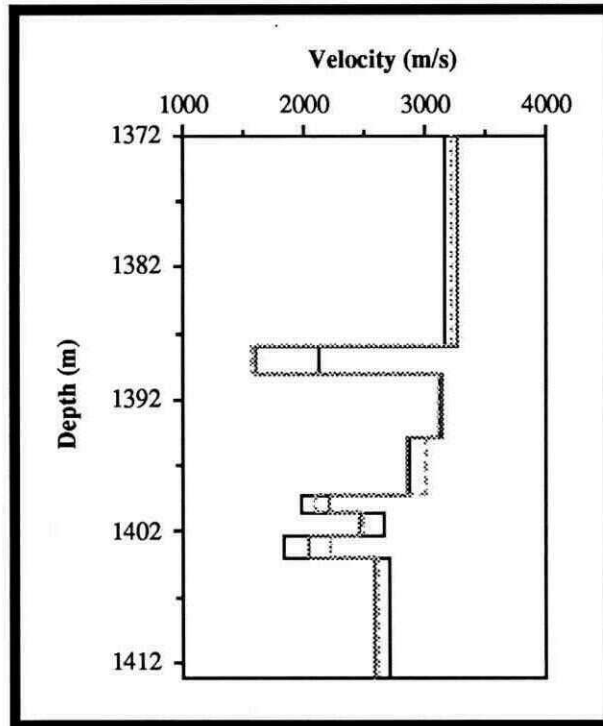


Figure 8: S-wave inversion of three independent receiver gathers

Another type of analysis is to take the estimated velocity of every interval and generate forward modelled, based on raytracing, direct arrivals for the geometry of the crosswell experiment. Then, compare the produced traveltimes to these originally observed (picked) on the real records. This would provide the response of every interval velocity, the one solution selected from the many solutions in every interval, with respect to the recorded data. Figures 10 and 11 show the comparison of the computed times with the observed ones. The raytracing algorithm implements the same two equations (1) and (2) discussed in earlier. The algorithm uses Newton's method in a forward modelling manner to capture the rays at the correct receiver location, within 0.1 cm (1 mm) tolerance. It mostly takes the raytracing algorithm 3 iterations to correctly compute the traveltimes of the direct arrivals. A receiver gather of 390 rays (source locations) takes less than 2 minutes of simulation on a Zenith-AT personal computer.

The results of Figures 10 and 11 have good agreement with the recorded times. Both Figures are consistent within themselves and even have the same behavior compared to each other in matching the observed times. At depth approximately 1388 m (the top of the thin shale unit), there is a drift between the traveltimes up to about 1386.5 m. It is very

invariable that the correct timing trend was missed while performing the interactive picking process. The agreement that follows the drift confirms that the estimated velocity is the correct answer since the zone from 1388 m and above to 1372 m represents only one layer in the model. Another explanation to consider is that if the observed traveltimes in the drift zone were correct, then they perhaps represent head waves that arrived earlier before the direct waves. It is then followed by the direct waves arriving first and this where the agreement recovers again.

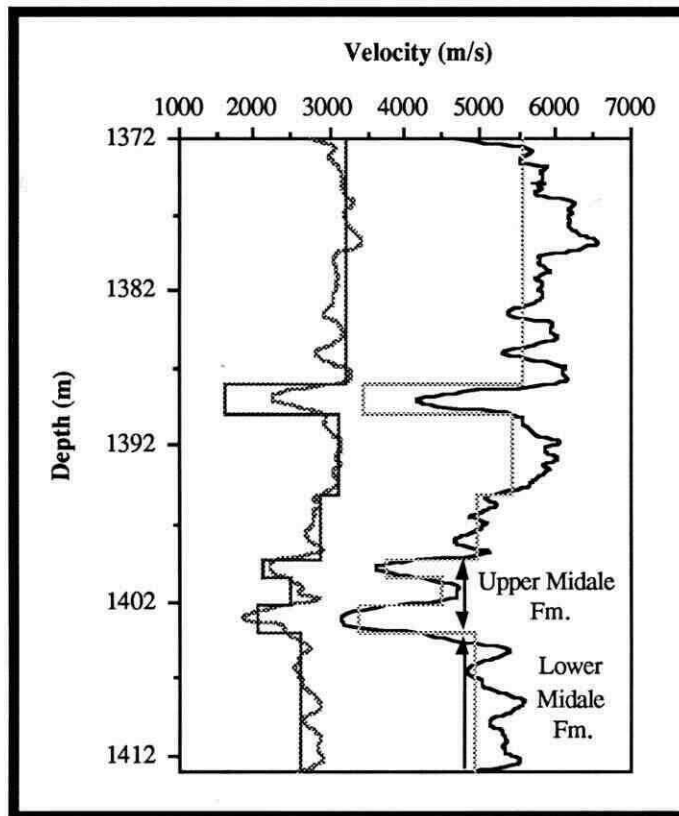


Figure 9: Comparison of P- and S-wave inversion results with the respective full-waveform velocity logs.

A final effort to study the inversion results is to look at the residual average error in every interval. This is done by computing the average error magnitude of the observed and computed traveltimes. The largest average error has been found in the S-wave case for the top interval (1372 m - 1388 m) where the error is computed to be 0.0000584 sec (0.0584 ms). That average error represents 0.936 percent of the average observed traveltimes in the respective interval. Similar computations for the percent of the average error with respect to the average observed traveltimes in all intervals of both P- and S-wave cases are carried out and found that the maximum error percent was 1.45 in an interval in the P-wave case.

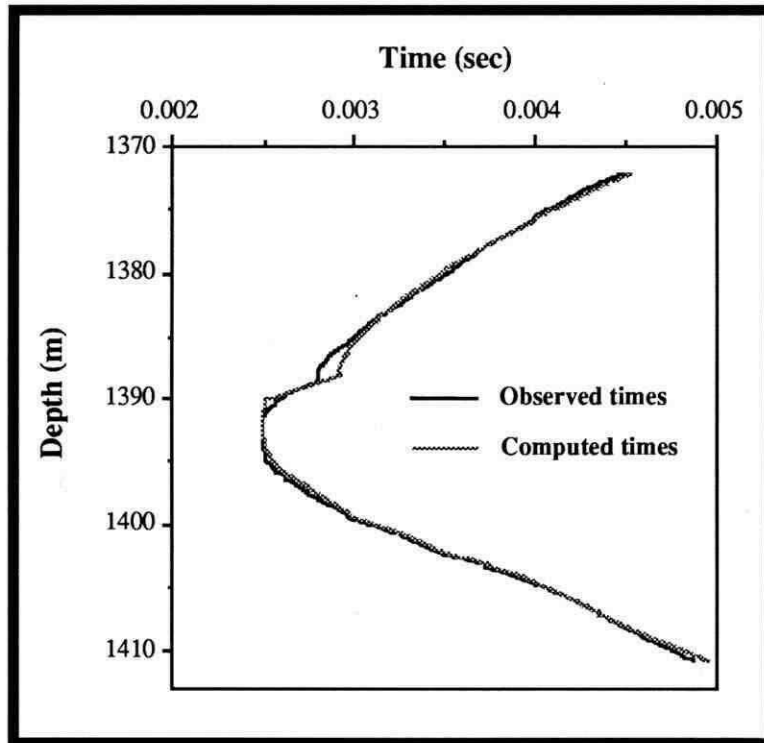


Figure 10: Comparison of the P-wave observed and computed direct arrivals. The computed traveltimes are obtained by forward modelling using the estimated velocities from the inversion.

2. Reflection processing

Up to this point, only direct arrivals of P and S waves have been used to obtain interval velocity information for the medium of propagation. The focus now is directed to the later arriving waves, namely, the reflected events.

As mentioned in the introductory literature review, a few studies have considered back scattered data through different migration algorithms to construct depth sections for the area between the boreholes (Zhu and McMechan, 1988; Hu et al., 1988a; Beydoun et al., 1989). The produced depth sections suffered serious artifacts as a result of the migration process applied.

To our knowledge, Baker and Harris (1984) and Iverson (1988) were the only two studies that transformed crosswell reflected events from the domain of field recording, receiver depth and time (z, t), to the domain of surface distance and subsurface depth (x, z) using the reconstruction technique of VSP data (Wyatt and Wyatt, 1984; Dillon and Thomson, 1984). This method made use of both upgoing and downgoing reflections present in crosswell data in order to produce a depth section that is similar to the classic surface seismic section. The two studies, however, had a critical assumption that is the reconstruction was based on a constant velocity model (straight raypath geometry). In hydrocarbon-producing subsurface, velocities usually vary considerably. This would in turn result considerable errors in depth placement of the reflectors.

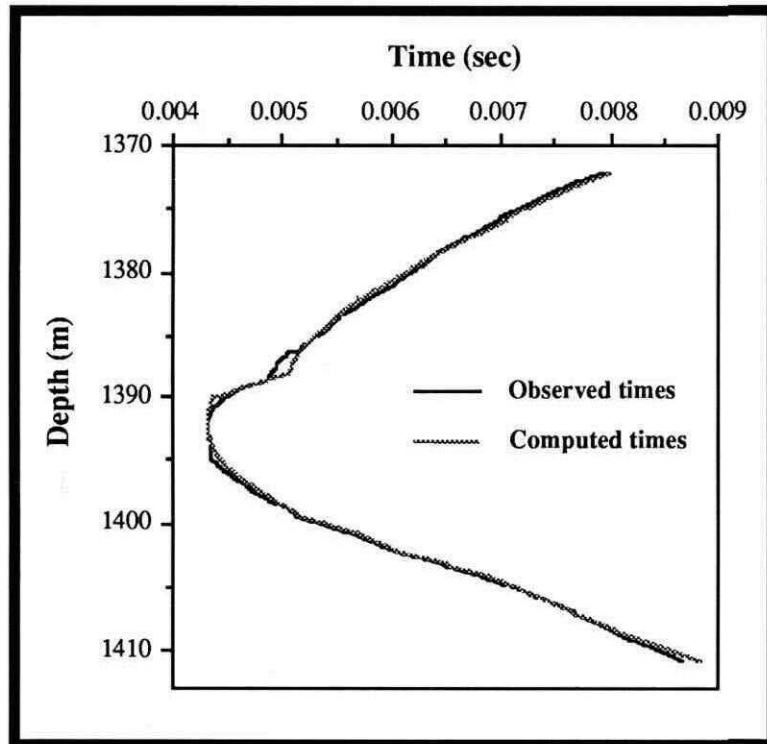


Figure 11: Comparison of the S-wave observed and computed direct arrivals. The computed traveltimes are obtained by forward modelling using the estimated velocities from the inversion.

This study is considered to be a continuation for the previous studies in terms of reflection processing of crosswell data. Effective wavefield separation techniques are implemented to enhance the reflected data. The crosswell coverage is introduced here based on constant-velocity model expressions which provide general subsurface locations at which reflected wavefields evolved. Also, proper transformation based on multi-layer model is discussed. Due to limitations in some of the software to process data with such fine sampling the field data (0.008 ms), scale factors are used to make the data look as they are 1 ms sampled. These scale factors do not affect any of the results obtained. The Figures of such results were then relabeled using true scales.

Figure 12 presents the processing flow conducted in this study for the crosswell field data. The following are the presentation and discussion of the results of every processing step with some review if necessary.

2.1 Preprocessing

The preprocessing step for the field data (9 receiver gathers) included trace balancing and band-pass filtering (Figure 4). Muting the direct arrivals of P waves down to the start of the direct arrivals of S waves is conducted following the band pass filtering as it is found that the reflected events are limited to S-wave modes. So, from now on, processing and its associated analysis would only be concerning S-wave reflections.

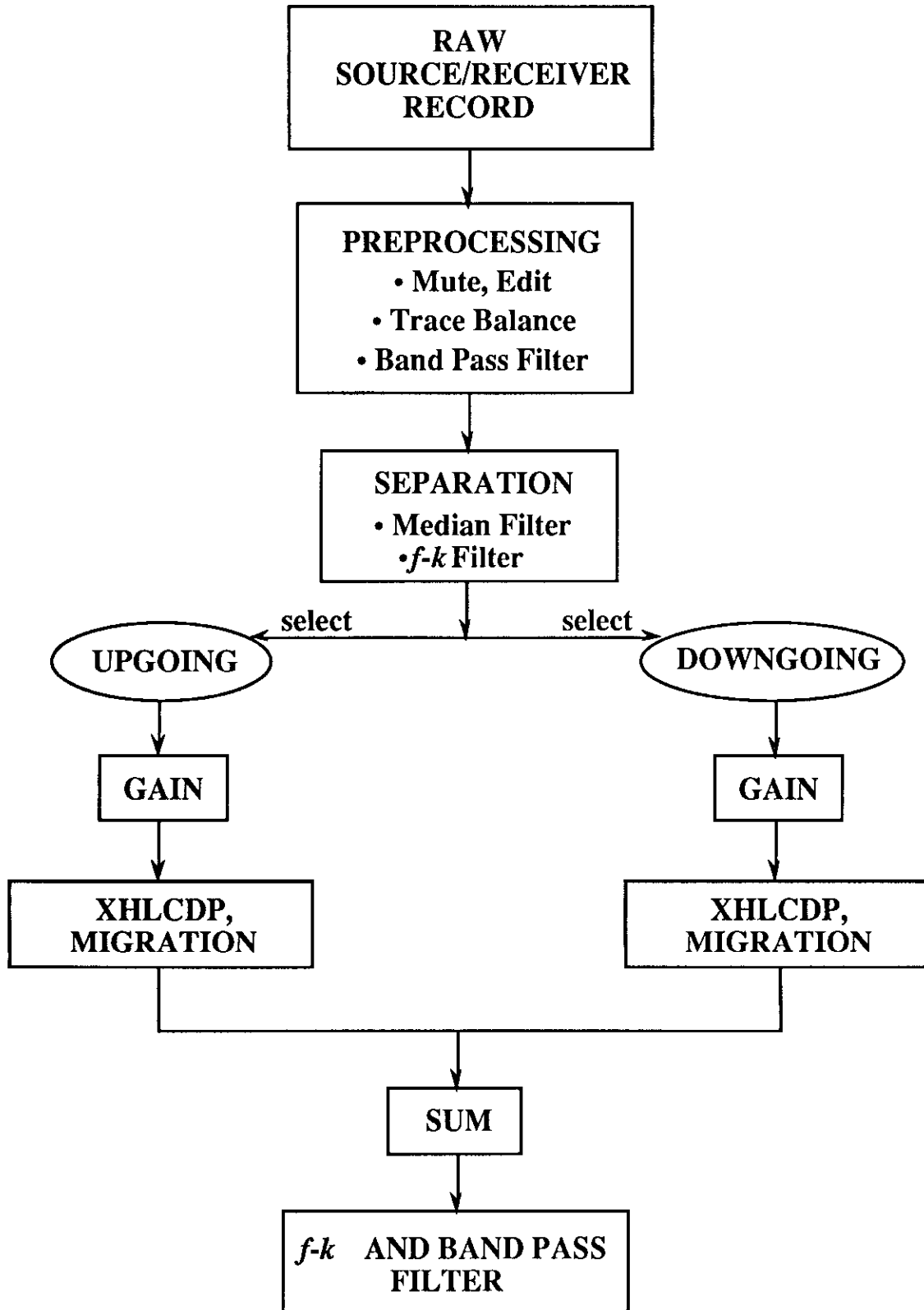


Figure 12: General processing flow of crosswell seismic data. All steps are used in this study except migration.

2.2 Wavefield separation

2.2.1 Median filtering

The first approach in processing the reflected arrivals involves application of the median filtering process. That is to remove the field-data strong shear direct arrivals which follow both upgoing and downgoing directions (Figure 4) with respect to the receiver location. Median filter is used to achieve such goals by enhancing certain arrivals and then subtracting them from the total record to yield the desired arrivals.

Median filters operate by selecting the middle value of an ascending-ordered sequence of numbers. These numbers are taken from a moving window on the data to be processed. Hardage (1985) and Stewart (1985) offer extended reviews of the median filtering process and its applications in processing seismic data. The operation is used to reject noisy spikes as well as enhance discontinuities in the data. It is proved to be very useful in Vertical Seismic Profile (VSP) and automatic editing of surface seismic data (Stewart, 1985). The running median filter can be applied along a given trace, or across adjacent traces. In general, a window of values will be used, a median extracted and placed on the output trace at the middle of the window. The process is repeated along the sequence until the entire sequence has been filtered.

Hardage (1985) gave considerable emphasis to the use of median filters in Vertical Seismic Profiling (VSP) data processing. He showed how they could be used to enhance events of interest. The method, removal of downgoing wave modes by subtraction, outlined by Hardage (1985) for VSP data is somewhat modified here to serve the purpose of removing the field-data direct arrivals from the later arriving reflections. Figures 13 and 14 show the filtered and difference records resultant from median filtering receiver gather 2 of the field data set (Figure 4) with 11-trace window starting with shear direct arrival times to the maximum trace length (9.6 ms). Effective direct arrivals removal can be seen on the filtered record (Figure 13) and much more stronger reflected events can now be traced with some other residual events on the difference record (Figure 14). Also, the median filter can create high frequency noise as can be observed particularly on the filtered record. A band-pass filter is usually used to remove these high frequencies introduced by the median filter.

A number of attempts were made to deconvolve the crosswell data. However, we found that deconvolution always degraded the reflections, so ultimately no deconvolution was used. The next step involves using 2-D (f - k) filters to separate the upgoing and downgoing reflections from each other to prepare them for further processing.

2.2.2 f - k dip filter

Like median filters, f - k dip filter is a multichannel process that operates on several data traces simultaneously. It is useful in discriminating against noise and enhancing signal on the basis of a criterion that can be distinguished from trace to trace, dip in this case. The term dip refers only to the apparent time dip of an event (measured in ms per trace) and not the spatial dip of the geologic structure. Here, the f - k filter is based on the concept that events with different dips that may interfere in the (t,z) domain can be isolated in the (f,k) domain. Thus, the operation requires the transformation of the data from the (t,z) into the (f,k) domain through the 2-D Fourier transform, two 1-D Fourier transforms.

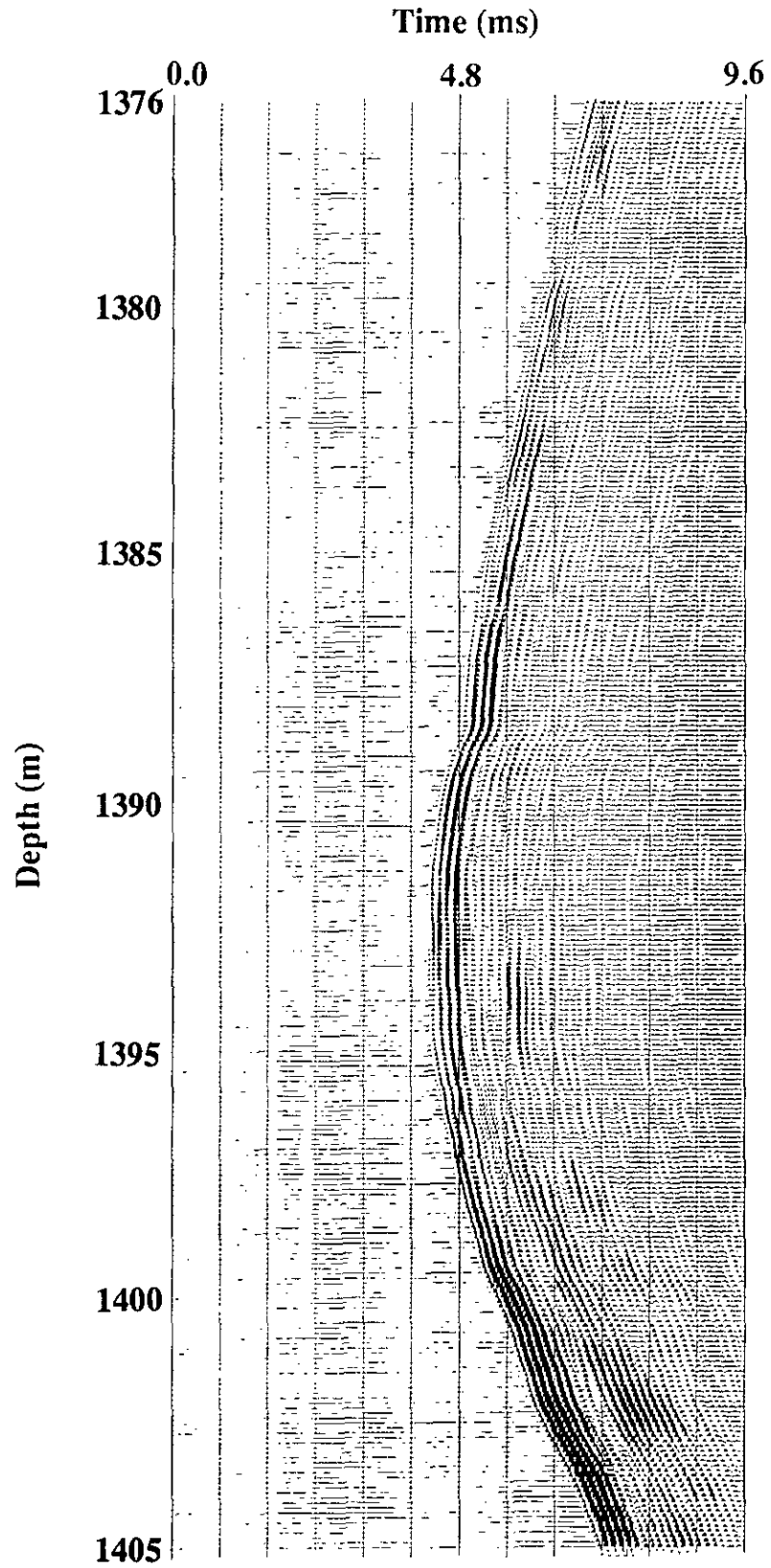


Figure 13: Filtered record (no. 2) of median filtering process designed on the S-wave arrivals.

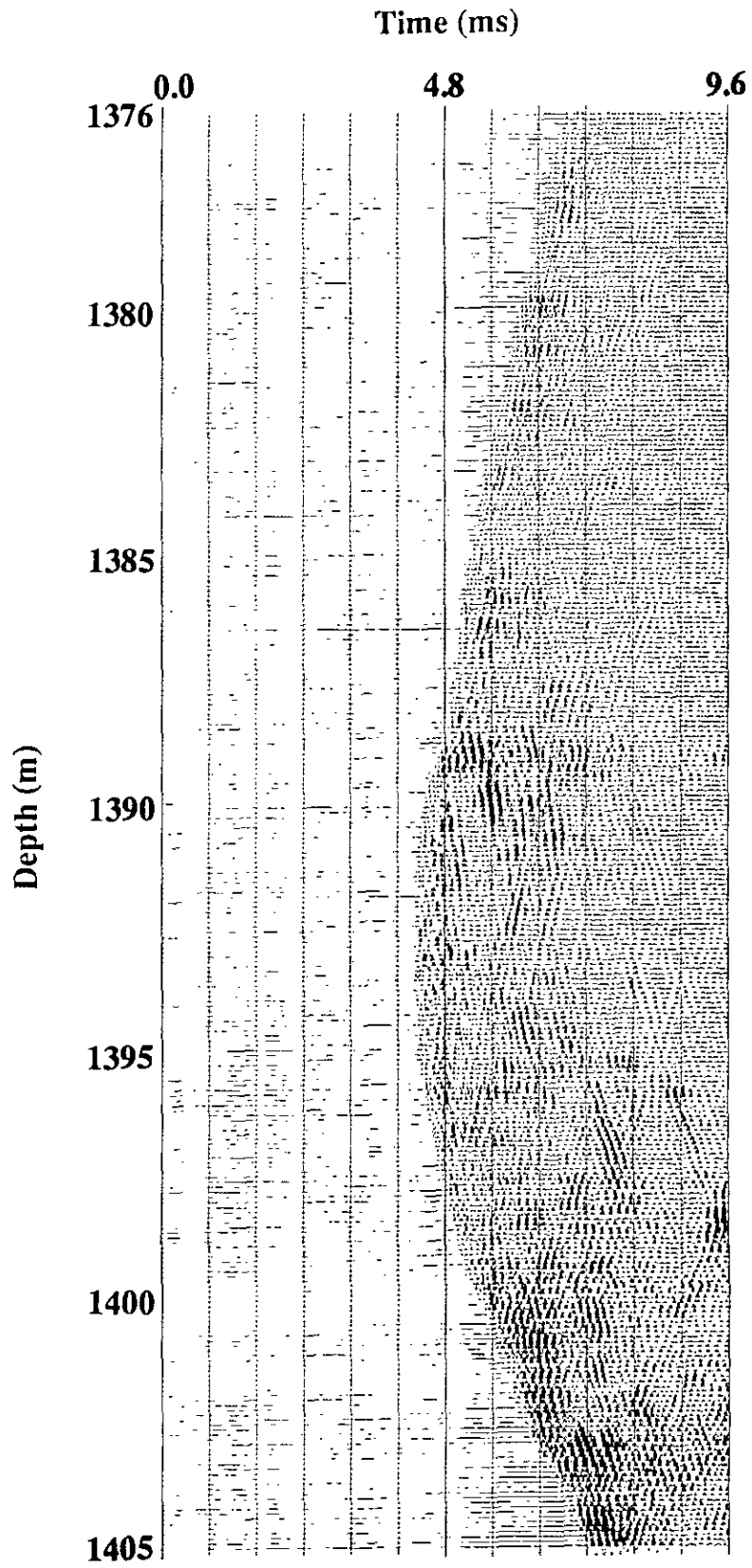


Figure 14: Difference record (no. 2) of median filtering process designed on the S-wave arrivals.

The purpose of using the f - k dip filter in this study is to separate the upgoing reflections from the downgoing ones since they have opposite dips. The convention used to determine the dip of each wave type is that an event has a positive dip if the reflection time decreases as the depth increases while an event has a negative dip if the reflection time increases as the depth increases. So, applying this rule on both wave types, upgoing (RUSS) and downgoing (RDSS), in Figure 4 indicates that downgoing events have positive dips while upgoing events have negative dips. Positive dips in the (t,z) domain are associated with positive wavenumbers in the (f,k) . Negative dips in the (t,z) domain are associated with negative wavenumbers in the (f,k) domain.

Yilmaz (1987) discusses the practical issues associated with the spatial aliasing, 2-D Fourier transform, and choice of pass/reject zones when performing f - k dip filtering. Removal of selected wave modes by the f - k filter in the case of Vertical Seismic Profiling (VSP) data is outlined by Hardage (1985). The process followed here would ultimately pass one wave type, say upgoing events (negative wavenumbers), while reject the other wave type, downgoing events (positive wavenumbers), completely from an input record that contains both of them, say the produced median filtered record after attenuating the direct arrivals. The same process is separately repeated with reversing the action of the filter with respect to the wave types for the same input record.

Taking the difference record (Figure 14) of median filtered field data to be the input record, the separated wavefields resulting from following such procedure independently for each wave type are shown in Figures 15 and 16 for upgoing and downgoing wavefields respectively. Numerous reflected events can now be seen on both records. As a reminder, these events represent symmetrical shear, S-S, reflections off the subsurface interfaces between the boreholes. There are few events that are separated correctly but do not follow that specific reflection raypath particularly in the lower part of the upgoing wavefield (about 1402 m - 1405 m). These are residual events on the difference record (Figure 14) resulting from the median filtering operation. Further processing of these crosswell data such as mapping, which involves a binning step, and summing different receiver maps should help to cancel these events out since they would not be correctly flattened as the primary reflections. In general, the reflections are prominent and promise good potential in further development. The next step is to gain these reflected data to make them more pronounced and continuous before attempting to map them.

2.3 Gain

The separated wavefields (Figures 15 and 16) need to be gained in terms of their amplitudes especially those of the reflections. This gives rise to time-variant gain, conventionally used in VSP and surface seismic data processing to compensate for amplitude decays resulting from geometrical spreading (Newman, 1973), transmission losses, and scattering (Hardage, 1985; Yilmaz, 1987). While reflections are brought up in strength, noise components in the data are also boosted. This is one undesirable aspect of any type of gain application (Yilmaz, 1987). A trace equalization process would be in order to balance the amplitudes of the record along the entire set of traces. This is particularly needed as can be noticed that the high amplitudes in Figures 15 and 16 would be even higher after the time-variant gain. Both time-variant gain and trace equalization are used here in this section for the purpose of preparing the reflected data for the mapping and summing process discussed later.

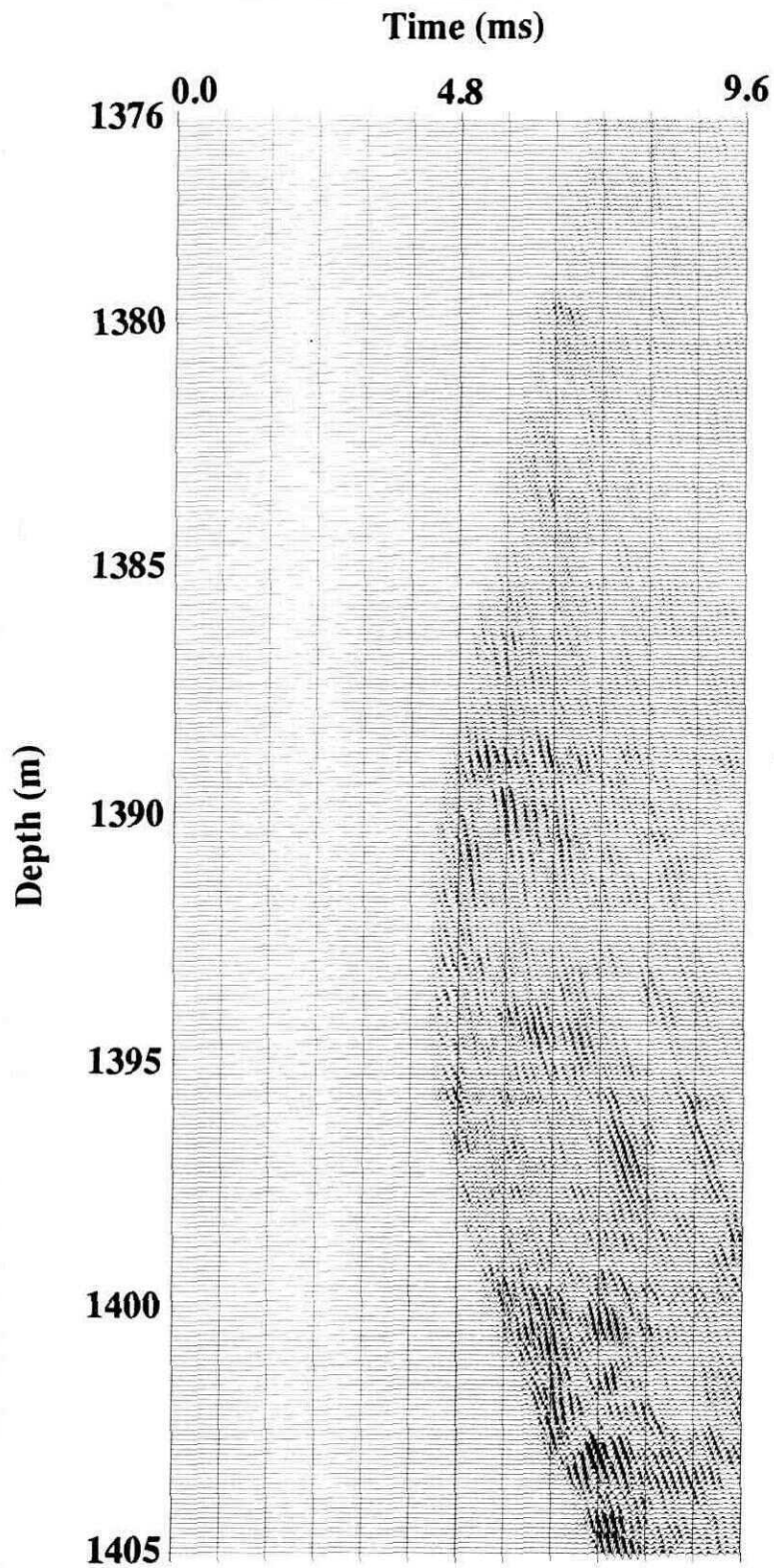


Figure 15: Upgoing reflected wavefield after f - k dip filtering the difference record in Figure 14.

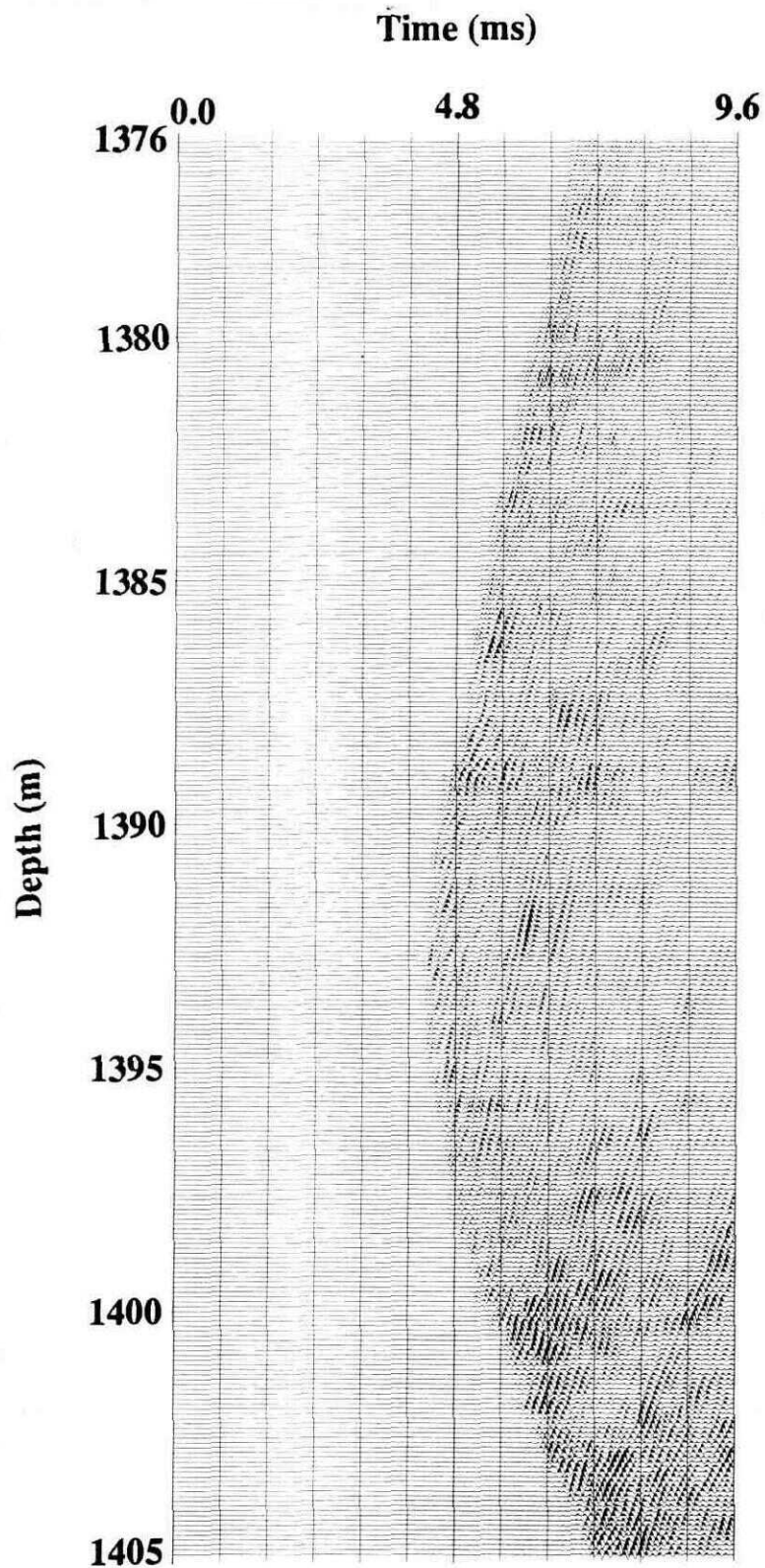


Figure 16: Downgoing reflected wavefield after f - k dip filtering the difference record in Figure 14.

2.3.1 Time-variant gain

Signal-level decay is evident in the separated records in Figures 15 and 16. Note the weak appearance of reflections particularly in source levels farther away from the receiver location (1392 m). This does not mean that there are no strong reflections present in these data. Because of the amplitude decay, low-level signal is recorded.

The gain function applied here is modified from (Hardage, 1985) in which the raw amplitudes $A(t)$ in every trace are multiplied by a gain function $G(t)$. That is

$$A_{\text{gained}}(t) = A(t) G(t), \quad (18)$$

where $G(t)$ has the form:

$$G(t) = \left(\frac{t}{c}\right)^x, \quad (19)$$

where t is time in ms, x is chosen from several tests to be 1.52 and c is a constant for normalizing purposes. Since we assume that the record contains only reflections, c was selected to be 4.3 ms as the earliest time of the data to gain. The results of applying such gain function on the data boosted up the residuals (noise component) left after the median filter as it boosted the primary reflections present.

2.3.2 Time-invariant balance

Trace balancing here is not really a gain, rather, it is simply balancing each trace in the group of traces in the record so that they all have the same desired rms amplitude level. The interest here is to bring down the signal level in the traces containing the high noise component while preserving the signal level in the traces containing the primary reflections. A trace balance scheme based on the peak amplitude criterion is performed here to obtain a separate scale factor for each trace. The scale factor, S , is given by

$$S = \frac{1.414}{A} r, \quad (20)$$

where A is that maximum absolute amplitude found on the entire input trace, and r is the desired rms amplitude for the output trace (consistently chosen as 2000). The entire trace is then multiplied by the computed scale factor.

The results of applying both the gain and balance steps on the separated upgoing and downgoing wavefields of Figures 15 and 16 are shown in Figures 17 and 18 respectively. Much more strong and continuous primary reflections can be seen along the entire record. In the same time, high-amplitude residuals of the median filter are heavily attenuated. The two points of interest stated above prove to be effectively achieved.

2.4 Crosswell transformation (XHLCDP)

This study considers a process conventionally known in VSP data processing as VSPCDP mapping (Wyatt and Wyatt, 1984; Dillon and Thomson, 1984). The interest here is to apply similar reconstruction procedure to crosswell reflected data and use its benefits in delineating the medium between the boreholes. The crosswell geometry is showed in

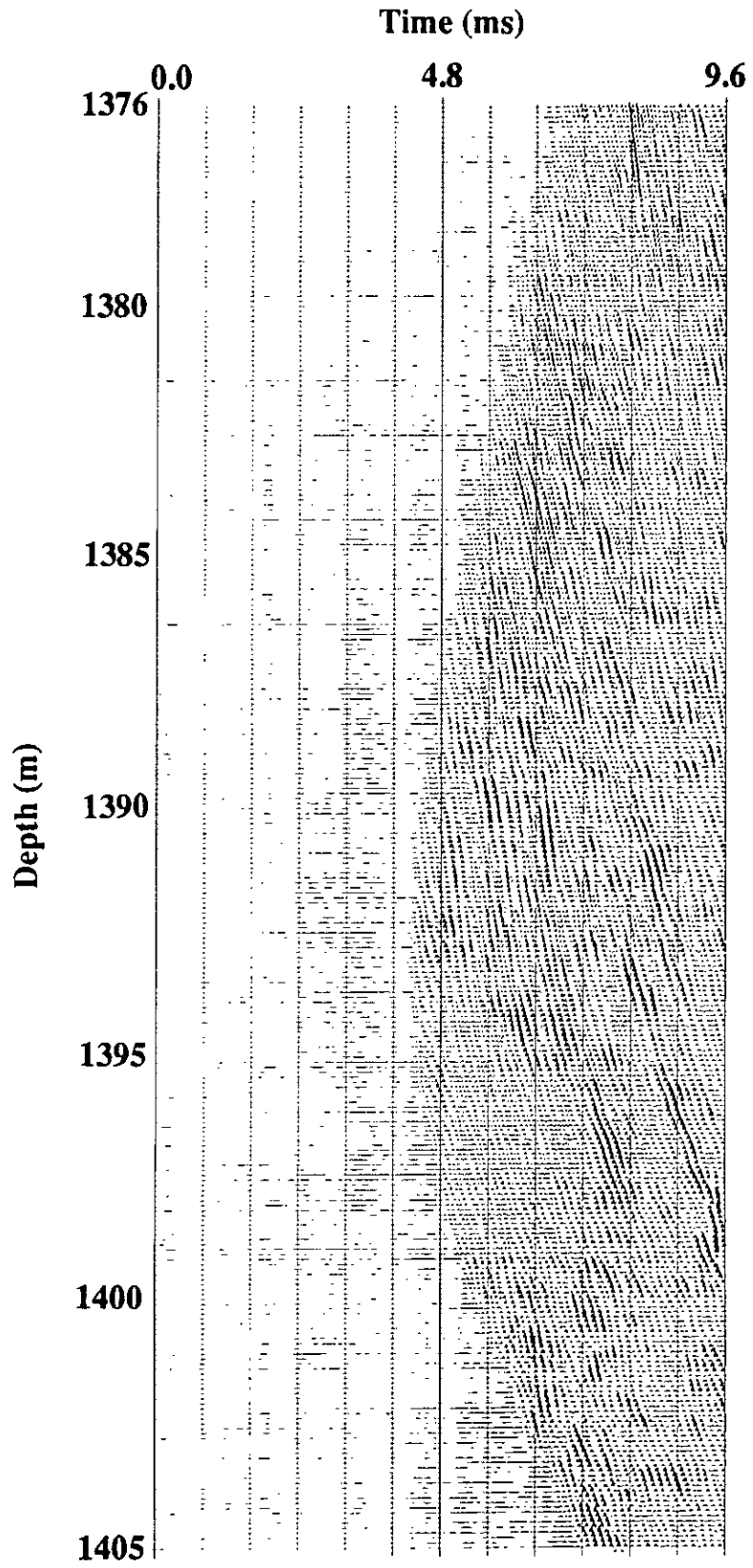


Figure 17: Gained upgoing reflected wavefield.

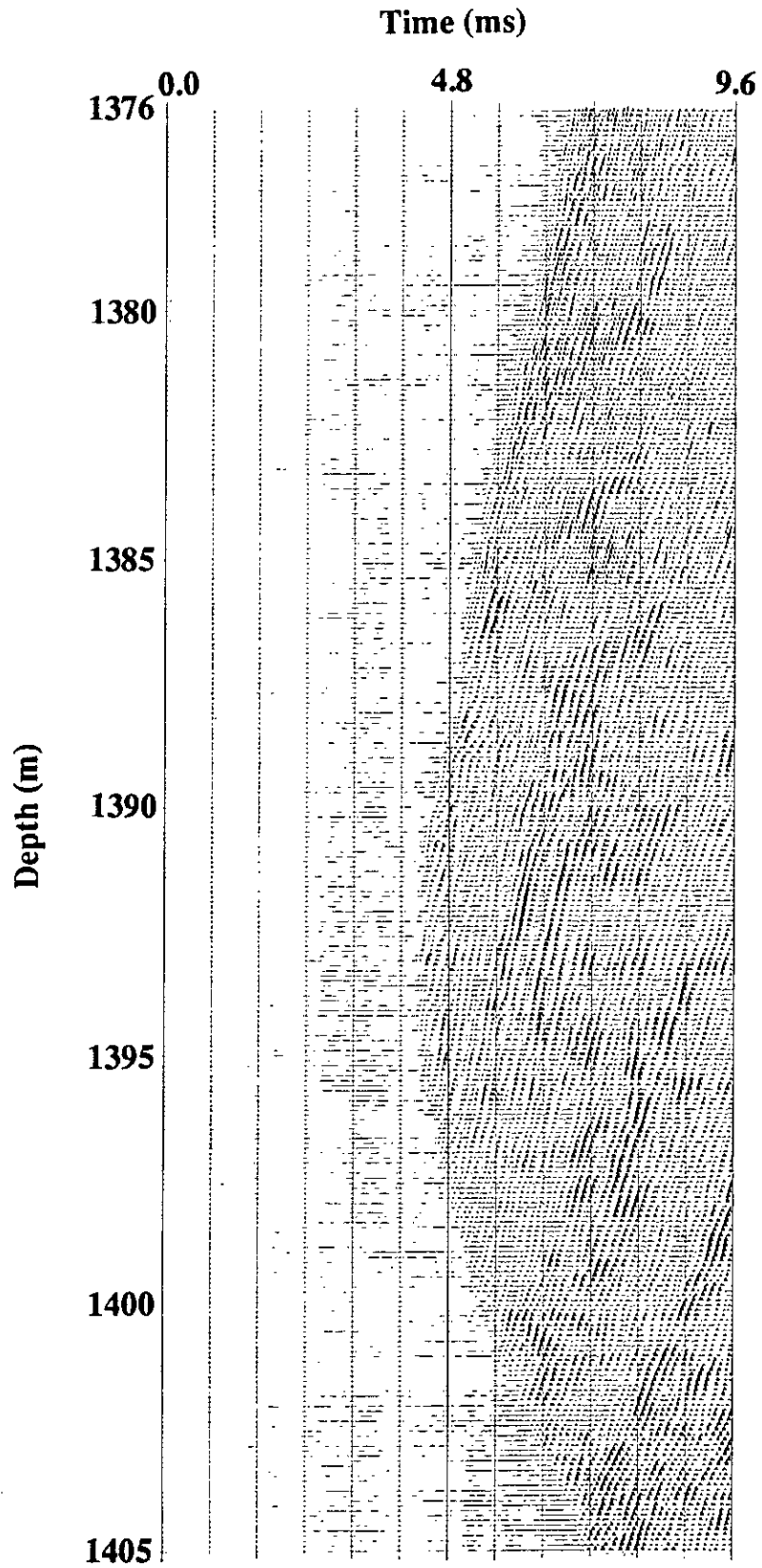


Figure 18: Gained downgoing reflected wavefield.

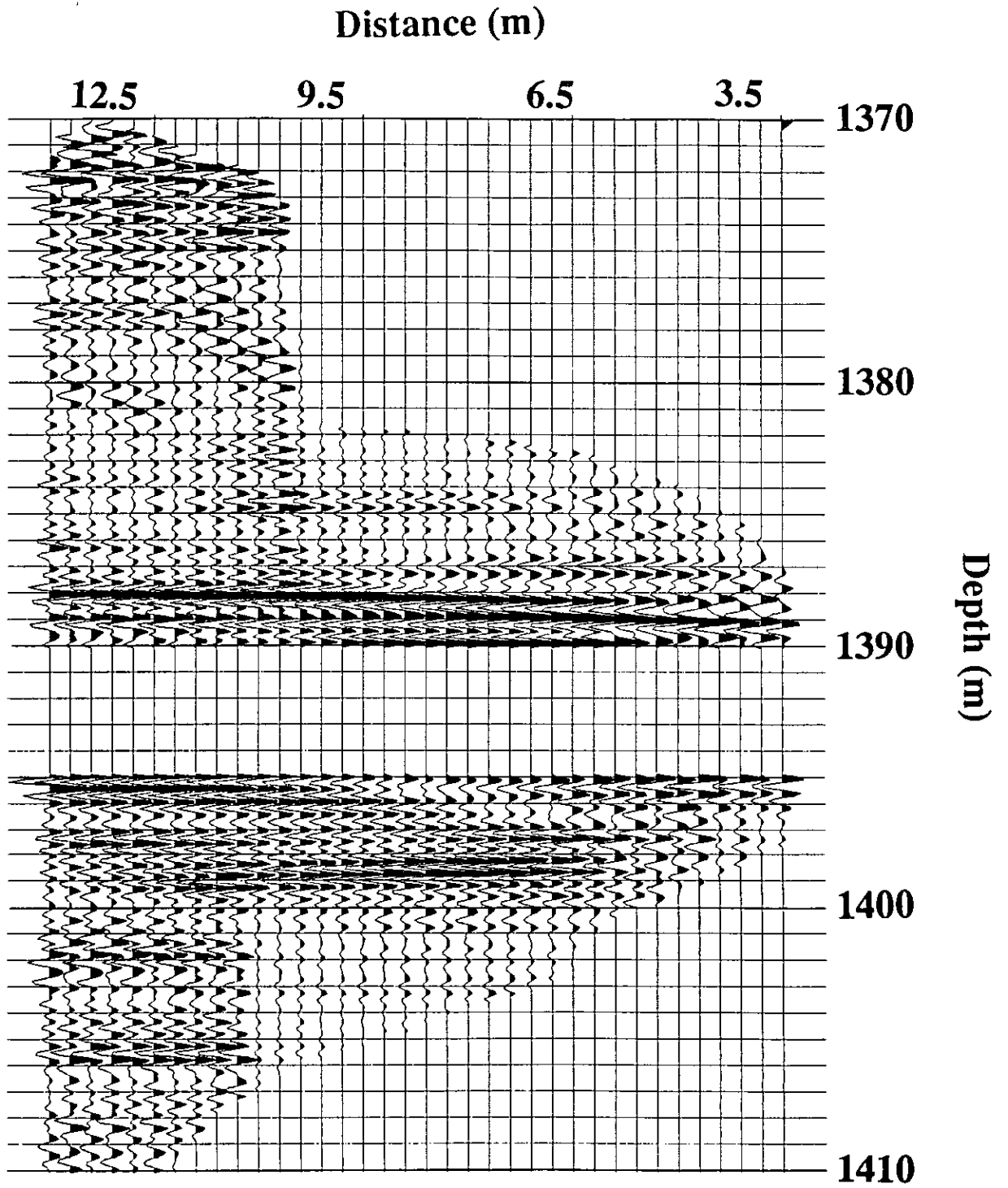


Figure 19: Final map of receiver gather no. 2. Upgoing and downgoing reflections are shown according to their subsurface depth.

Abdalla et al. (1989) to have a subsurface coverage that extends beyond the midpoint between the boreholes. It also includes primary reflections in the downgoing direction as well as the upgoing one.

The current study demonstrates crosswell mapping based on a multi-layered model with its proper transformation attributes (Abdalla et al., 1990). This may represent an advantage over the two previous studies (Baker and Harris, 1984; Iverson, 1988) that considered a constant-velocity model in their transformation process. Here, the mapping procedure is called XHLCDP transformation to indicate that upgoing and downgoing primary reflections are used. The reconstruction is separately performed on both the upgoing and the downgoing reflected wavefields (Figures 17 and 18) based on the shear velocity profile obtained from the traveltime inversion procedure presented here in this study.

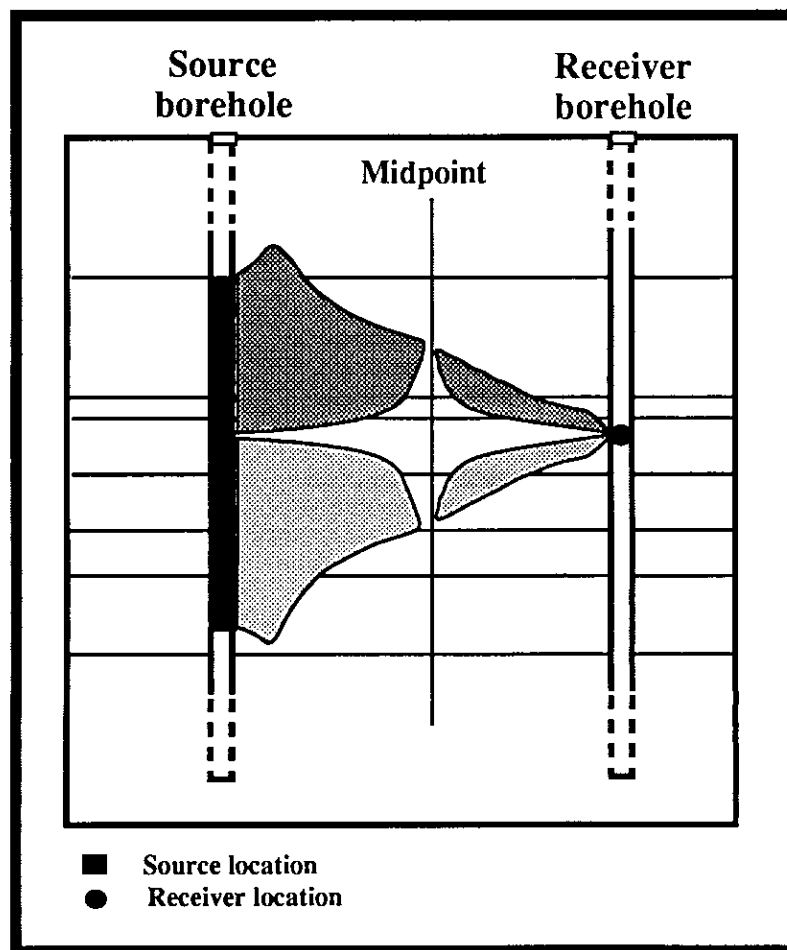


Figure 20: Subsurface coverage of receiver gather #2. Note the effect of limited recording time on the coverage.

Further poststack processing is carried out on the mapping results to finally produce the reflected image in Figure 19. These poststack processes include:

- Mute of the noisy zone around the receiver location that has no reflectivity coverage as seen in the approximate subsurface coverage (Figure 20).

- f - k dip filter to enhance primary reflections.
- High cut band-pass filter to remove high frequency noise components.
- Automatic gain control (AGC) to help continue the events.

It should be noted that the cut-off apparent on the boundaries of the image (Figure 19) is the result of the limited recording time of the field experiment. Figure 20 depicts the approximate form of the mapped record. It is very critical when acquiring crosswell data and reflections are of interest to record the maximum points possible. This would provide as a better reflected image with higher fold as possible.

2.5 Sum

At this point, the several maps of the crosswell data are individually reconstructed. Since the area of subsurface coverage depends on the source/receiver array, it is of interest to sum all maps of each data set and form one composite reflection image of the subsurface between the boreholes. This should also provide the maximum subsurface coverage for both upgoing and downgoing wavefields. The summing procedure is conducted accordingly to keep the amplitude level the same in the final map. The sum is normalized by the number of live samples added together.

The sum of the nine receiver maps is shown in Figure 21 for depth interval 1370 m to 1420 m. One advantage of the sum is the contribution of the other maps into the muted zone, 1390 m - 1395 m, of the single receiver map shown in Figure 19. In fact, this is another reason for muting the zone around the receiver location that does not exhibit any reflected energy. That is if the muted data were summed to other maps that show primary reflections, the stack would have been erroneous. The other advantage is that there are three overlapping intervals produced from the mapping of the different receiver gathers. These intervals, when stacked together, give an interval of 1370 m to 1440 m. Figure 21 is only shown down to 1420 m. There is a mute zone starting at 1418 m that had no coverage. No more maps are available to overlap in this area.

The lateral illumination of the image extends along most of the subsurface, 3.0 m to 13.5 m from the receiver borehole with bin width of 0.3 m. In addition, and perhaps the most significant achievement of that image is the vertical resolution ability. Events can be seen within an interval less than 1 m (about 0.5 m).

There is however one drawback in the image resulting from the summing process. There is a considerable degradation in some of the events after the sum. Note the weaker event in the final image (Figure 21) at about 1388 m compared to its corresponding strength before the sum (Figure 19). Other events exhibit similar effects of the destructive interference as seen in the final image at depth about 1401 m. The direct reason for such interference is that similar events in the different maps are not exactly located at the same depth. This is probably due to two reasons. The first is that the velocity-constructed model from the inversion results is not perfect for all the different maps. The second reason goes back to the unconfirmed source/receiver locations in the field experiment. Finally, the presence of the noisy dipping trend in the final section (Figure 21) at depth about 1405 m on the right side of image and depth 1420 m on the left side is a result of single fold coverage.

2.6 Instantaneous amplitude

The high cut band-pass filter used to produce the map of Figure 19 is designed to obtain a smooth representation of the reflected data. However, the wavelet sharpness maintained after the band-pass filter seems to destructively affect the sum of the final map (Figure 21).

Seeking a localized measure of the reflectivity strength along the depth interval of the final maps, instantaneous amplitude sections are computed using the method of complex attributes (Taner, 1978). In short, the seismic trace is represented as a complex function $u(t)$,

$$u(t) = x(t) + i y(t), \quad (21)$$

where $x(t)$ is the seismic trace itself and $y(t)$ is its quadrature. The quadrature is a 90-degree phase-shifted version of the recorded trace. It is obtained by taking the Hilbert transform of $x(t)$ (Bracewell, 1965; Yilmaz, 1987). The instantaneous amplitude, $R(t)$, computed from

$$R(t) = [x^2(t) + y^2(t)]^{\frac{1}{2}}. \quad (22)$$

is proportionally related to the square root of the total energy of the seismic trace at an instant of time.

Figure 22 shows the reflectivity strength of the final sum of maps (Figure 21) respectively. A general smoothed description of the reflectivity is now obtained maintaining the high resolution content (about 1 m) of the images.

INTERPRETATION

Our final goal is to interpret the pictures that have been made. Shown in Figures 21 and 22 are the final depth images (map and its envelope) along with the shear velocity log recorded in well FS-1 (source borehole) and a synthetic seismogram in depth for the same depth interval. The generated synthetic seismogram has similar frequency content as the image. The synthetic seismogram has been converted from time to depth using the sonic velocity function, shown on the left of both Figures. So, we can see that there is a built-in difference in the velocity functions used to construct the synthetic seismogram and the reflected image. This difference can appear as a traveltime mismatch when comparing the two data types. The other theoretical principle that the synthetic is based on is the assumption of normal incidence reflectivity. That assumption may not be valid for the crosswell image since its transformation is performed based on nonnormal incidence using raytracing.

With the previous assumptions in mind, the correlation between the synthetic seismogram and the reflected images is carried out and several horizons are identified. Of these horizons, the tops of shale and other interbeds in the Ratcliffe beds formation, and the top and an interbed interface in the marly dolomite, upper Midale formation. Although similar band-pass filter is used in both the synthetic seismogram and the crosswell field data, inspecting the two final Figures 21 and 22 suggest that the crosswell images contain data with higher resolution than that of the synthetic seismogram obtained from the sonic log.

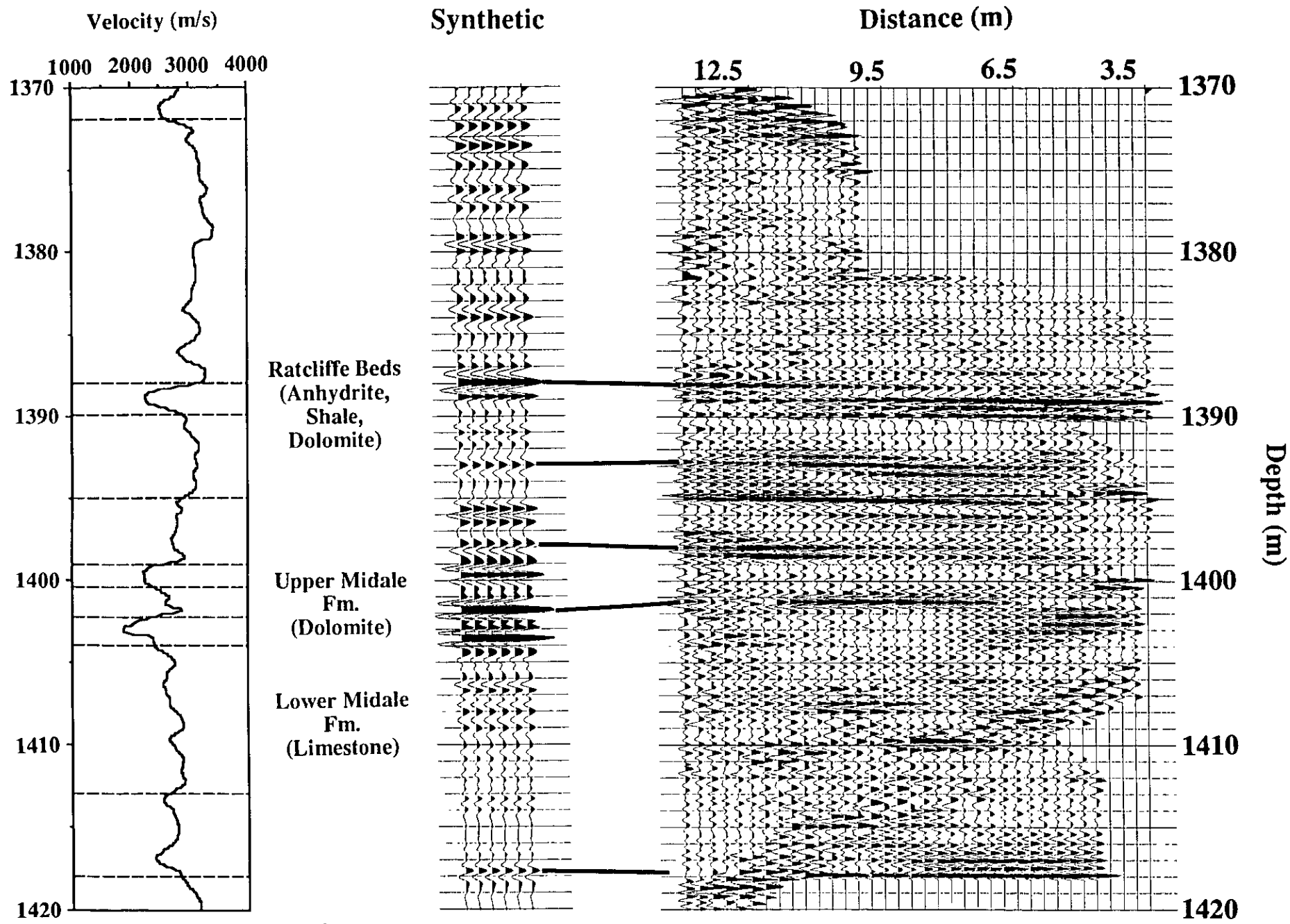


Figure 21: Correlation between the sum of all receiver-gather maps (right) and the synthetic seismogram in depth (middle) generated from the sonic log (left).

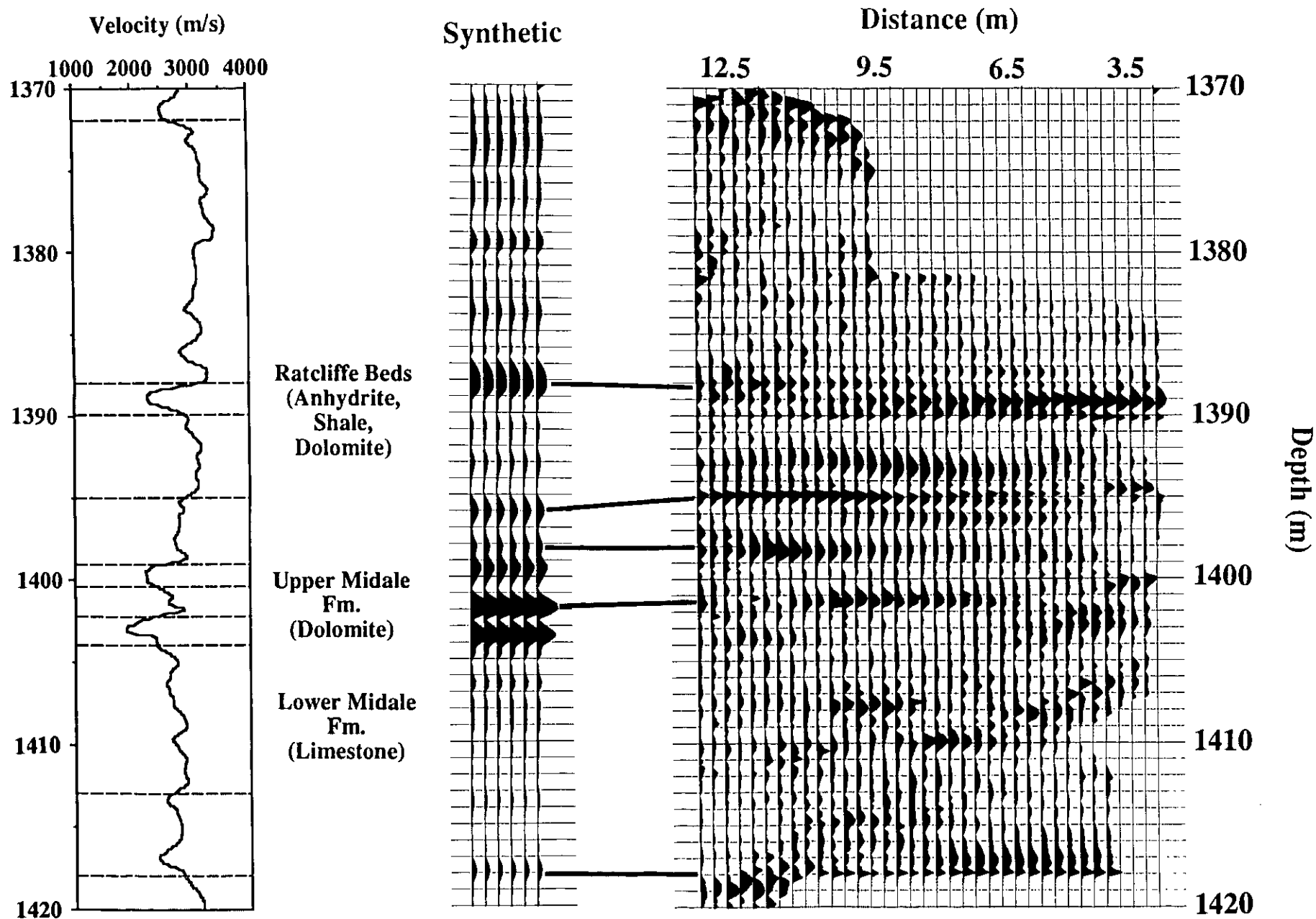


Figure 22: Correlation between the instantaneous amplitudes of the sum (right) and the synthetic seismogram in depth (middle) generated from the sonic log (left).

As discussed earlier in the sum processing step, there are some event degradations in the final total maps due to event interference. Even before the sum, the individual map showed the high-frequency primary events concentrating in different parts of the image. The reflected image itself is currently investigated in terms of the event amplitude changes with vertical offset. These AVO changes may well be significant as the crosswell geometry gives rise to large (and variable) angles of incidence.

CONCLUSIONS

Inverting crosswell P- and S-wave direct arrivals produces background or macro-scopic velocity maps. These are found to be consistent with log interval velocities. The crosswell data in this study contain primary reflected shear waves in both upgoing and downgoing directions. Processing such waves does not need special software development. It can be performed using the conventional borehole software. Transforming (XHLCDP) these reflected wavefields using the seismic velocities obtained from the inversion technique gives high resolution images of the subsurface between the boreholes, particularly the zone of interest. Crosswell geometry is shown to have an extended subsurface coverage away from the borehole which can complement the interpretation of well logs and VSP data. An interpretable image can be reconstructed from the reflection data.

ACKNOWLEDGMENTS

The authors of this paper wish to thank Shell Canada for releasing the log and crosswell data used in this study. The processing presented here was conducted at Western Geophysical Company, Canada. Many thanks to Roger Hawthorne, Bill Rimmer, Adam Chow and Lynn Burroughs of Western Geophysical for their generous assistance. We would also like to express our appreciation to the sponsors of the CREWES Project for their support.

REFERENCES

- Abdalla, A. A. and Stewart, R. R., 1989, Reflection processing of synthetic crosshole data: paper 16, presented at the First Annual Meeting of the CREWES Project, Banff, Alberta, 225-244.
- Abdalla, A. A., Stewart, R. R., and Henley, D. C., 1990, Traveltime inversion and reflection processing of cross-hole seismic data: paper BG2.8, presented at the 60th Annual Meeting of SEG, San Francisco, 47-50.
- Baker, L. J. and Harris, J. M., 1984, Cross-Borehole Seismic Imaging: paper BHG2.2, presented at the 1984 Annual Meeting of SEG, Atlanta, 23-25.
- Banik, N. C., 1984, Velocity anisotropy of shales and depth estimation in the North Sea basin: *Geophysics*, 49, 1411-1419.
- Beydoun, W. B., Delvaux, J., Mendes, M., Noual, G., and Tarantola, A., 1989, Practical aspects of an elastic migration/inversion of crosshole data for reservoir characterization: A Paris basin example: *Geophysics*, 54, 1587-1595.
- Bois, P., La Porte, M., Lavergne, M., and Thomas, G., 1972, Well-to-well seismic measurements: *Geophysics*, 37, 471-480.
- Bracewell, R., 1965, *The Fourier transform and its applications*: McGraw-Hill Book Co.
- Bregman, N. D., Hurley, P. A., and West, G. F., 1989, Seismic tomography at a fire-flood site: *Geophysics*, 54, 1082-1090.

- Burden, R. L. and Faires, J. D., 1985, Numerical analysis: PWS publishers.
- Dillon, P. B. and Thomson, R. C., 1984, Offset source VSP surveys and their image reconstruction: *Geophys. Prosp.*, 32, 790-811.
- Esmersoy, C., 1990, Inversion of P and SV waves from multicomponent offset vertical seismic profiles: *Geophysics*, 55, 39-50.
- Fehler, M. and Pearson, C., 1984, Cross-hole seismic surveys: Applications for studying subsurface fracture systems at a hot dry rock geothermal site: *Geophysics*, 49, 37-45.
- Geis, W. T., Stewart, R. R., Jones, M. J., and Katopodis, P. E., 1990, Processing, correlating, and interpreting converted shear waves from borehole data in southern Alberta: *Geophysics*, 55, 660-669.
- Hamming, R. W. and Feigenbaum, 1971, Introduction to applied numerical analysis: McGraw-Hill Book Co.
- Hardage, B. A., 1985, Vertical Seismic Profiling: Geophysical Press, 14A.
- Hornby, B. E., 1989, Imaging of near-borehole structure using full-waveform sonic data: *Geophysics*, 54, 747-757.
- Hu, L., McMechan, G. A., and Harris, J. M., 1988a, Acoustic prestack migration of cross-hole data: *Geophysics*, 53, 1015-1023.
- Hu, L., McMechan, G. A., and Harris, J. M., 1988b, Elastic finite-difference modeling of cross-hole seismic data: *Bull. Seis. Soc. Am.*, 78, 1796-1806.
- Ivansson, S., 1985, A study of methods for tomographic velocity estimation in the presence of low-velocity zones: *Geophysics*, 50, 969-988.
- Iverson, W. P., 1988, Crosswell Logging for Acoustic Impedance: *Pet. Tech. J.*, 75-82.
- Justice, J. H., 1986a, Travelttime inversion for flat-layer model: *Geophysics*, 51, 1904-1911.
- Justice, J. H., 1986b, Interval velocity analysis from VSP surveys: *J. Can. Soc. Expl. Geophys.*, 22, 33-43.
- Justice, J. H., Vassiliou, A. A., Singh, S., Logel, J. D., Hansen, P. A., Hall, B. R., Hutt, P. R., and Solanki, J. J., 1989, Acoustic tomography for monitoring enhanced oil recovery: *The Leading Edge*, 8, no. 2, 12-19.
- Lines, L. R. and LaFehr, E. D., 1989, Tomographic modeling of a cross-borehole data set: *Geophysics*, 54, 1249-1257
- Macrides, C. G., 1987, Seismic tomography in oil sands for monitoring thermal recovery processes: Ph. D. thesis, Physics Department, University of Alberta.
- Macrides, C. G., Kanasewich, E. R., and Bharatha, S., 1988, Multiborehole seismic imaging in steam injection heavy oil recovery projects: *Geophysics*, 53, 65-75.
- Marzetta, T. L., Orton, M., Krampe, A., Johnston, L. K., and Wuenschel, P. C., 1988, A hydrophone vertical seismic profiling experiment: *Geophysics*, 53, 1437-1444.
- Newman, P., 1973, Divergence effects in a layered earth: *Geophysics*, 38, 481-488.
- Peterson, J. E., Paulsson, B. N. P., and McEvelly, T. V., 1985, Applications of algebraic reconstruction techniques to crosshole seismic data: *Geophysics*, 50, 1566-1580.
- Poel, N. J. van der and Cassell, B. R., 1989, Borehole seismic surveys for fault delineation in the Dutch North Sea: *Geophysics*, 54, 1091-1100.
- Pratt, R. G. and Worthington, M. H., 1988, The application of diffraction tomography to cross-hole seismic data: *Geophysics*, 53, 1284-1294.
- Slotnik, M. M., 1959, Lessons in seismic computing: *Soc. Expl. Geophys.*
- Stewart, R. R., 1985, Median filtering: Review and a new f/k analogue design: *J. Can. Soc. Expl. Geophys.*, 21, 54-63.
- 1988, VSPCDP map for P waves: Personal communication.
- 1989, Integrated seismic analysis: Kidney area, northern Alberta, Canada: *Geophysics*, 54, 1240-1248.
- Taner, M. T., 1978, Complex seismic trace analysis: *Geophysics*, 44, 1041-1063.
- Winterstein, D. F. and Paulsson, B. N. P., 1990, Velocity anisotropy in shale determined from crosshole seismic and vertical seismic profile data: *Geophysics*, 55, 470-479.
- Wyatt, K. D. and Wyatt, S. B., 1984, Determining subsurface structure using the vertical seismic profiling: In Toksoz, M. N., and Stewart, R. R., Eds, Vertical seismic profiling: Advanced concepts, Geophysical Press.
- Yilmaz, O., 1987, Seismic data processing: *Soc. Expl. Geophys.*
- Zhu, X., and McMechan, G. A., 1988, Acoustic modeling and migration of stacked cross-hole data: *Geophysics*, 53, 492-500.